Geochimica et Cosmochimica Acta 358 (2023) 77–92

Contents lists available at ScienceDirect

Geochimica et Cosmochimica Acta

journal homepage: www.elsevier.com/locate/gca

Dual carbonate clumped isotopes (Δ_{47}-Δ_{48}) constrains kinetic effects and timescales in peridotite-associated springs at the Cedars, Northern California

Zeeshan A. Parvez [a,b,c,1], Jamie K. Lucarelli [a,b,1], Irvin W. Matamoros [a,b], Joshua Rubi [b,d], Kevin Miguel [b,d], Ben Elliott [a,b], Randy Flores [a,b], Robert N. Ulrich [a,b], Robert A. Eagle [b,e,f], James M. Watkins [g], John N. Christensen [h], Aradhna Tripati [a,b,e,f,*]

[a] Department of Earth, Planetary, and Space Sciences, University of California, Los Angeles, CA, USA
[b] Center for Diversity and Leadership in Science, University of California, Los Angeles, CA, USA
[c] Department of Chemistry and Biochemistry, University of California, Los Angeles, CA, USA
[d] East Los Angeles College, Los Angeles, CA, USA
[e] Department of Atmospheric and Oceanic Sciences, University of California, Los Angeles, CA, USA
[f] Institute of Environment and Sustainability, University of California, Los Angeles, CA, USA
[g] Department of Earth Sciences, University of Oregon, Eugene, OR, USA
[h] Department of Energy Geosciences, Lawrence Berkeley National Laboratory, Berkeley CA, USA

ARTICLE INFO

Associate editor: Frank McDermott

Keywords:
Serpentinization
Peridotite
Clumped isotopes
Carbon sequestration
Kinetic isotope effects

ABSTRACT

The Cedars is an area in Northern California with a chain of highly alkaline springs resulting from CO_2-charged meteorological water interacting with a peridotite body. Serpentinization resulting from this interaction at depth leads to the sequestration of various carbonate minerals into veins accompanied by a release of Ca^{2+} and OH^- enriched water to the surface, creating an environment which promotes rapid precipitation of $CaCO_3$ at surface springs. This environment enables us to apply the recently developed Δ_{47}-Δ_{48} dual clumped isotope analysis to probe kinetic isotope effects (KIEs) and timescales of CO_2 transformation in a region with the potential for geological CO_2 sequestration. We analyzed $CaCO_3$ recovered from various localities and identified significant kinetic fractionations associated with CO_2 absorption in a majority of samples, characterized by enrichment in Δ_{47} values and depletion in Δ_{48} values relative to equilibrium. Surface floes exhibited the largest KIEs ($\Delta\Delta_{47}$: 0.163‰, $\Delta\Delta_{48}$: −0.761‰). Surface floe samples begin to precipitate out of solution within the first hour of CO_2 absorption, and the dissolved inorganic carbon (DIC) pool requires a residence time of >100 h to achieve isotopic equilibria. The Δ_{48}/Δ_{47} slope of samples from the Cedars (−3.223 ± 0.519) is within the range of published theoretical values designed to constrain CO_2 hydrolysis-related kinetic fractionation (−1.724 to −8.330). The $\Delta_{47}/\delta^{18}O$ slope (−0.009 ± 0.001) and $\Delta_{47}/\delta^{13}C$ slope (−0.009 ± 0.001) are roughly consistent with literature values reported from a peridotite in Oman of −0.006 ± 0.002 and −0.005 ± 0.002, respectively. The consistency of slopes in the multi-isotope space suggests the Δ_{47}-Δ_{48} dual carbonate clumped isotope framework can be applied to study CO_2-absorption processes in applied systems, including sites of interest for geological sequestration.

1. Introduction

The rate and mechanism of CO_2 transformation into carbonate minerals in natural alkaline springs and peridotites is of interest because of the potential for permanent, non-toxic CO_2 sequestration. Carbon mineralization at peridotite bodies that host alkaline springs occur worldwide. It is hypothesized that serpentinization, a process that involves the hydration of ultramafic minerals, facilitates the carbon mineralization process in peridotite (Bruni et al., 2002; Falk et al., 2016; García del Real et al., 2016; Suzuki et al., 2017; de Obeso and Kelemen,

* Corresponding author at: Department of Earth, Planetary, and Space Sciences, University of California, Los Angeles, CA, USA.
E-mail address: atripati@g.ucla.edu (A. Tripati).
[1] Joint first author.

https://doi.org/10.1016/j.gca.2023.06.022
Received 12 July 2022; Accepted 20 June 2023
Available online 24 June 2023

2018). Serpentinization can be generally described by reactions (1)–(3) listed below (Kelemen and Matter, 2008).

$$2Mg_2SiO_4 + Mg_2Si_2O_6 + 4H_2O \rightarrow 2Mg_3Si_2O_5(OH)_4 \quad (1)$$

$$Mg_2SiO_4 + 2CO_2 \rightarrow 2MgCO_3 + SiO_2 \quad (2)$$

$$Mg_2SiO_4 + CaMgSi_2O_6 + 2CO_2 + 2H_2O \rightarrow 2Mg_3Si_2O_5(OH)_4 + CaCO_3 + MgCO_3 \quad (3)$$

Olivine (Mg_2SiO_4) and pyroxene ($Mg_2Si_2O_6$; $CaMgSi_2O_6$) react with CO_2-charged water to form serpentine [$Mg_3Si_2O_5(OH)_4$], magnesite ($MgCO_3$), quartz (SiO_2), calcite ($CaCO_3$), and aragonite ($CaCO_3$). Relatively small amounts of hydromagnesite [$Mg_5(CO_3)_4(OH)_2{\cdot}4H_2O$] (Zedef et al., 2000), brucite [($Mg(OH)_2$] (Moody, 1976), nitromagnesite [$Mg(NO_3)_2$] (Schefer and Grube, 1995), and nesquehonite ($MgCO_3{\cdot}3H_2O$) (Kastrinakis et al., 2021) may also form via reactions (4)–(7), respectively.

$$5Mg^{2+} + 4CO_3^{2-} + 2OH^- + 4H_2O \rightarrow Mg_5(CO_3)_4(OH)_2{\cdot}4H_2O \quad (4)$$

$$2Mg2SiO_4 + 3H_2O \rightarrow Mg_3Si_2O_5(OH)_4 + Mg(OH)_2 \quad (5)$$

$$2MgO + 4NO_2 + O_2 \rightarrow 2\ Mg(NO_3)_2 \quad (6)$$

$$Mg^2 + +CO_2 + 4H_2O \rightarrow MgCO_3{\cdot}2H_2O + 2H^+ \quad (7)$$

Ongoing serpentinization of mantle peridotite bodies by meteoric waters can be identified by highly alkaline water in proximate springs, stable isotope ratios of precipitated carbonate minerals, the formation of travertines, and carbonate veins in the hosting peridotite body (Bruni et al., 2002; Cipolli et al., 2004).

Early research on ultramafic formations undergoing serpentinization led to a conceptual model for this process (Barnes and O'Neil, 1969) (Fig. 1). Meteoric groundwater charged with atmospheric CO_2 reacts with the peridotite body near the surface and forms water that is rich in Mg^{2+} and HCO_3^-, termed Type 1 waters (Barnes and O'Neil, 1969). As this water moves underground and encounters the peridotite body, the serpentinization process is catalyzed by CO_2-charged H_2O, leading to the precipitation of $MgCO_3$ and $CaCO_3$ into veins in the peridotite. A sharp elevation in pH accompanies the mineral precipitation due to the enrichment of the water solution with OH^- anions, termed Type 2 water. This Type 2 water also exhibits significant enrichment in Ca^{2+} and depletion in DIC. Type 2 water is brought up to the surface where it interacts with Type 1 water, instantly supersaturating the fluids with respect to carbonate and leading to the precipitation of calcite, aragonite, and travertine in surface springs.

A potential tool for probing carbon mineralization in these settings is carbonate clumped isotope geochemistry. The measurement of carbonate clumped isotopes in minerals precipitated from alkaline fluids can potentially constrain the mechanism(s) of kinetic isotope effects (KIEs) and rate of precipitation (Tripati et al., 2015; Watkins and Hunt, 2015; Guo, 2020; Bajnai et al., 2020). Carbonate clumped isotope analysis measures the abundance of CO_2 molecules with multiple heavy isotope substitutions, where the CO_2 is produced from the acid digestion of carbonate minerals. When carbonate minerals form at thermodynamic equilibrium, they have a temperature-dependent preference of heavy isotope aggregation based on relative zero-point energies (Ghosh et al., 2006; Schauble et al., 2006). The abundance of the most common multiply-substituted mass 47 ($^{13}C^{18}O^{16}O$) and mass 48 ($^{12}C^{18}O^{18}O$) isotopologues are given by Eqs. (8) and (9),

$$\Delta_{47} = (R47_{sample}/R47_{stochastic} - 1) \quad (8)$$

$$\Delta_{48} = (R48_{sample}/R48_{stochastic} - 1) \quad (9)$$

where Ri is the ratio of the minor isotopologues (m/z 47 or m/z 48) relative to the most abundant isotopologue (m/z 44). $Ri_{stochastic}$ is calculated using the measured abundance of $^{13}C/^{12}C$ and $^{18}O/^{16}O$ (R^{18}) in the sample and the estimated abundance of $^{17}O/^{16}O$ (Eiler, 2007). The latter ratio is estimated from R^{18} assuming a mass-dependent

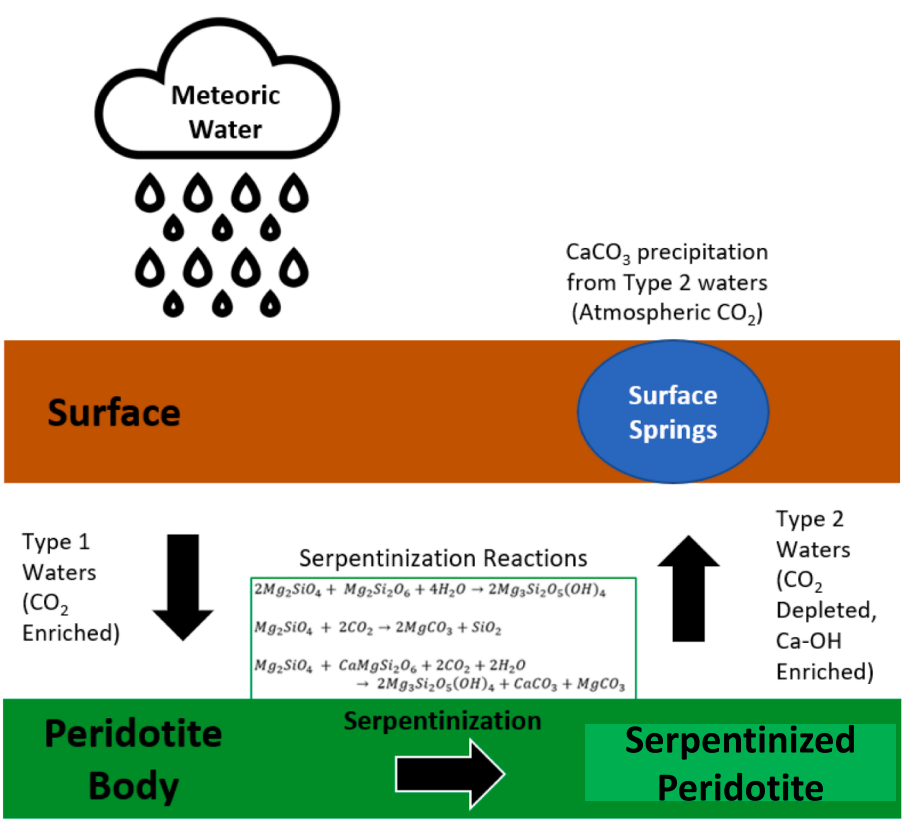

Fig. 1. Processes associated with CO_2 absorption and transformation at The Cedars. Surface waters from meteoric sources that are enriched with CO_2 from the atmosphere seep into the ground and interact with ultramafic peridotite, forming "Type 1" waters enriched in Mg^{2+} and HCO_3^-. Through a series of serpentinization reactions (reactions (1)–(3)), various carbonate minerals precipitate and are sequestered in pores and fractures resulting in veins in the peridotite body. Reaction by-products are ejected into pore waters, creating waters which are enriched in Ca^{2+} and OH^- ions, and depleted in CO_2 ("Type 2" waters), which are then shuttled to the surface. Type 1 and Type 2 waters interact at the surface in the presence of atmospheric CO_2, resulting in rapid precipitation of $CaCO_3$. Terminology from Barnes and O'Neil (1969).

relationship between ^{18}O and ^{17}O (Daëron et al., 2016). The Δ_{47} and Δ_{48} values are given in parts per thousand (permil, ‰) (Eiler and Schauble, 2004; Ghosh et al., 2006; Eiler, 2007).

To date, most studies mechanistically exploring KIEs in carbonate minerals using clumped isotopes have focused on isotopic disequilibria in paired Δ_{47} and oxygen isotope ($\delta^{18}O$) signatures. Diffusion has been hypothesized to produce KIEs in Δ_{47}-$\delta^{18}O$ in atmospheric CO_2 and corals (Eiler and Schauble, 2004; Thiagarajan et al., 2011). KIEs in biotic and abiotic systems associated with (de)hydration and (de)hydroxylation reactions can drive deviations from Δ_{47} equilibrium (Ghosh et al., 2006; Guo et al., 2009; Saenger et al., 2012; Falk et al., 2016; Spooner et al., 2016), as can CO_2 degassing, which has been used to explain Δ_{47} disequilibrium in speleothems (Hendy, 1971; Affek et al., 2008; McDermott et al., 2011; Guo and Zhou, 2019). Tang et al. (2014) hypothesized that kinetic fractionation observed in inorganic calcite precipitation experiments at pH $\geq$ 10 occurred due to the DIC pool not having sufficient time to achieve isotopic equilibrium prior to mineral precipitation, and DIC speciation favoring CO_3^{2-} at higher pH.

Previously, Δ_{47} values have been used to study CO_2 absorption-dominant disequilibria processes. Falk et al. (2016) reported data from carbonate minerals in hyperalkaline springs at the Oman ophiolite and attributed disequilibria to the increase in CO_2 absorption in water at elevated pH. This study showed that carbonate minerals from these highly alkaline systems exhibit significant increases in Δ_{47}, accompanied by decreases in $\delta^{18}O$ and $\delta^{13}C$. The observed pattern was found to be consistent with CO_2 absorption-driven disequilibrium processes related to the CO_2 hydroxylation reaction being expressed (Falk et al., 2016).

Recent work has shown that the "dual" carbonate clumped isotope system, the paired measurement of Δ_{47} and Δ_{48}, has a characteristic relationship to equilibrium and can be used to study KIEs (Tripati et al., 2015; Fiebig et al., 2019; Guo, 2020; Bajnai et al., 2020; Lucarelli et al., 2023). The equilibrium Δ_{47}-Δ_{48} dual clumped isotope relationship was constrained by theory (Hill et al., 2014; Tripati et al., 2015; Guo, 2020; Hill et al., 2020) and more recently, by measurements from multiple studies (Fiebig et al., 2019, 2021; Bajnai et al., 2020; Lucarelli et al., 2023). However, the use of dual clumped isotope measurements for mechanistic identification of KIEs is limited. The basis relies on theoretical modeling (Hill et al., 2014; Tripati et al., 2015; Guo, 2020; Hill et al., 2020) to constrain KIEs in Δ_{47}, Δ_{48}, and $\delta^{18}O$ in HCO_3^- and CO_3^{2-} from DIC-H_2O exchange driven disequilibria pathways, and (de)hydration and (de)hydroxylation reactions occurring during CO_2 absorption and CO_2 degassing. Applications to identify KIEs has been limited to a small number of measurements from biominerals including warm and cold-water coral, belemnite, and brachiopods, as well as speleothems (Bajnai et al., 2020; Lucarelli et al., 2023).

Here, we apply the novel dual carbonate clumped isotope approach, which combines the measurement of Δ_{47} and Δ_{48}, to carbonate minerals from alkaline springs at The Cedars, located in a coastal mountain range formed of peridotite in Northern California. The high alkalinity, elevated pH of 11.5, and low dissolved [CO_2] facilitate the uptake of CO_2 (Lívanský, 1982; Devriendt et al., 2017), which participates in hydration or hydroxylation reactions leading to the formation of HCO_3^- (reactions (10) and (11)). These two reactions are the most important in understanding $^{18}O/^{16}O$ isotopic equilibration as they provide the only route for the direct exchange of O atoms between H_2O and DIC (Zeebe and Wolf-Gladrow, 2001). Reactions (12)–(14) show the pathway from HCO_3^- to CO_3^{2-} and splitting of water molecules, and reactions (15)–(16) result in carbonate mineral formation. Reactions (10)–(16) contribute to isotopic equilibration of DIC in an aqueous solution.

$$CO_2 + H_2O \leftrightarrow H_2CO_3 \leftrightarrow HCO_3^- + H^+ \quad (10)$$

$$CO_2 + OH^- \leftrightarrow HCO_3^- \quad (11)$$

$$HCO_3^- + OH^- \leftrightarrow H_2O + CO_3^{2-} \quad (12)$$

$$HCO_3^- \leftrightarrow H^+ + CO_3^{2-} \quad (13)$$

$$H_2O \leftrightarrow H^+ + OH^- \quad (14)$$

$$Ca^{2+} + HCO_3^- \leftrightarrow CaCO_3 + H^+ \quad (15)$$

$$Ca^{2+} + CO_3^{2-} \leftrightarrow CaCO_3 \quad (16)$$

The amount of time required for clumped and oxygen isotopic equilibrium to be achieved is governed by the temperature-dependent forward and reverse rate constants for the hydration and hydroxylation reactions, as well as DIC speciation (Zeebe and Wolf-Gladrow, 2001). DIC speciation is a function of temperature and pH (Uchikawa and Zeebe, 2012; Tripati et al., 2015). At pH > 10, similar to what is observed in waters in peridotite bodies such as The Cedars, the time to reach equilibration is significantly increased due to DIC speciation being dominated by CO_3^{2-}, resulting in low concentrations of CO_2 remaining for isotopic exchange reactions (10) and (11) (Beck et al., 2005; Tripati et al., 2015; Weise and Kluge, 2020). If the DIC pool does not have sufficient time to achieve isotopic equilibrium before precipitation begins, disequilibrium isotopic compositions may be recorded in the mineral during precipitation reactions (15) and (16).

In this study, our goal is to use multiple isotope systems including dual clumped isotopes (Δ_{47}, Δ_{48}) and bulk stable isotopes ($\delta^{18}O$, $\delta^{13}C$) to mechanistically evaluate disequilibria, examine the origin of KIEs in DIC and carbonate minerals, and study the timescales associated with mineral precipitation. Our measurements are combined with modeling to study DIC and mineral isotopic evolution. Finally, we compare our results to published work from other peridotite bodies and evaluate our approach for its potential use in geological CO_2 sequestration applications.

2. Methods

2.1. The Cedars samples

The Cedars is part of the Northern California Coastal Mountain Range and is located at N38°37′14.84″/W123°08′02.13 (Fig. 2). The Cedars is inside of a 700 km long surrounding body of ultramafic rocks called the Coast Range Ophiolite (CRO). The broader Coastal Mountain Range consists of peridotites in contact with part of the Franciscan Subduction Complex (FSC). The FSC consists of primarily greywacke-type sandstone, greenstone, radiolarian chert, and minor foraminiferal limestone (Blake et al., 2012). The peridotite body has an approximate surface area of 22.4 km^2 (3.5 km width, 6.4 km length) and extends 1–2 km below the surface (Coleman, 2000). The peridotite body consists primarily of olivine, orthopyroxene, and clinopyroxene in varying proportions as harzburgite (75% olivine and 25% orthopyroxene/clinopyroxene) and dunite (100% olivine) (Coleman, 2000). Interactions between the peridotite body and groundwaters derived from multiple sources has resulted in serpentinization of 5–20% of the ultramafic body, particularly around the perimeter that is in contact with the FSC, where the perimeter is predominantly composed of sheared serpentine (Coleman, 2000; Blake et al., 2012).

Groundwater discharge from the ultramafic body is highly alkaline, enriched in Ca^{2+} and OH^-, and is brought to the surface through various springs in the area (Coleman, 2004; Sleep et al., 2004) where it mixes with relatively neutral pH surface waters charged with atmospheric CO_2 at an elevation between ~275 and 335 m above sea level (Barnes and O'Neil, 1969; Morrill et al., 2013).

The samples used for this study are comprised of $CaCO_3$ and were collected from The Cedars by Christensen et al. (2021), spanning eight visits in 2013, 2014, 2016, and 2018. Four major sites seen in Fig. 2 were sampled: NS1 "Wedding Cake" (samples: A, Q), The Barnes Spring Complex (BSC) (samples: AA, Alpha, C1, P, PA-C2, PB-C2, PE-C2, PE-C3, S, T1, T2, T3a, T3b, T4, T5, U, V, X), Grotto Pool Springs (GPS) (samples:

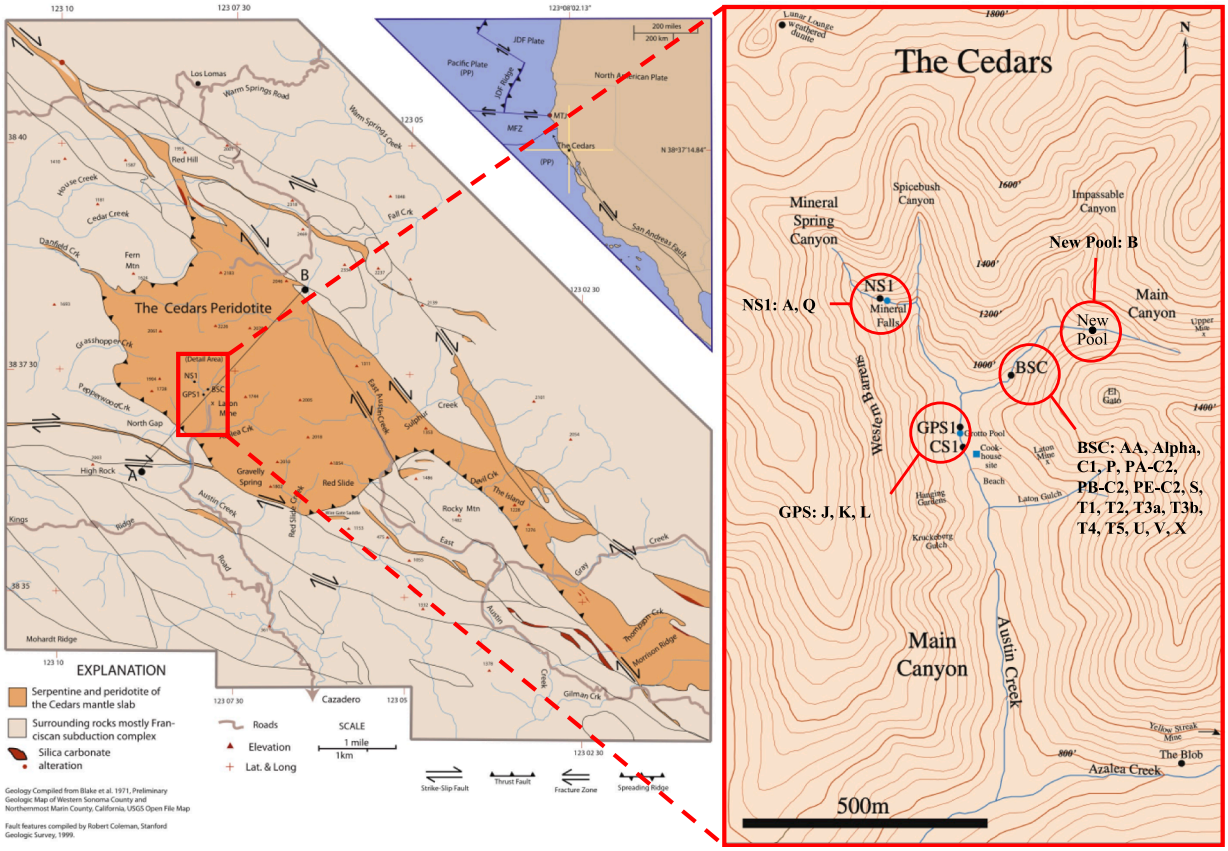

Fig. 2. Map of The Cedars site showing the sample locations. Sample locations indicated in the right panel include NS1 (samples: A, Q,), Grotto Pool Springs (GPS) (samples: J, K, L), Barnes Spring Complex (BSC) (samples: AA, Alpha, C1, P, PA-C2, PB-C2, PE-C2, PE-C3, S, T1, T2, T3a, T3b, T4, T5, U, V, X), and New Pool (sample: B). The "Wedding Cake" is at the NS1 location above the Mineral Falls. Modified from Morrill et al. (2013) and Christensen et al. (2021).

J, K, L), and the "New Pool" (sample: B). The "Wedding Cake" is at the NS1 location above the Mineral Falls. The $CaCO_3$ samples were collected from several different localities adjacent to the springs seen in Fig. 2: (1) partially consolidated materials from rims of pools; (2) precipitates from the surface of pools, also known as floes; (3) dendritic forms and encrustations from sites of creek-spring mixing; (4) unconsolidated material, also known as snow, from the bottom of the pools; and (5) solid, old travertine deposits, taken as a hand sample representing different layers, collected from the BSC. Any consolidated, or partially consolidated surface materials were skimmed from the surface or captured on screens based on the location they were collected from. Specific sample information, including composition and location of recovery, is listed in Table 1. The terminology used to describe samples in this paper is after Christensen et al. (2021).

Water samples from the high pH springs were taken using a 0.22 μm Millipore filter unit, acidified to a pH of 2 using HNO_3, and collected in high-density polyethylene (HDPE) bottles (Christensen et al., 2021). The pH of the water was measured on site using a Thermo-Scientific, Orion hand-held pH meter. Temperature measurements were taken of the water source at the time of carbonate sample recovery (Christensen et al., 2021).

2.2. Analysis and instrumentation

All clumped isotopic measurements were made in the Eagle-Tripati laboratory using two Nu Instruments Perspective isotope ratio mass spectrometers (IRMS) with methods described in detail in prior publications (Upadhyay et al., 2021; Lucarelli et al., 2023). Here we will refer to the first IRMS as Nu Perspective-1, and the second as Nu Perspective-2a and Nu Perspective-2b, as measurements on the latter instrument used two configurations. Both instruments and all configurations have been shown to produce statistically indistinguishable Δ_{47} (Upadhyay et al., 2021; Lucarelli et al., 2023) and Δ_{48} values (Lucarelli et al., 2023), with standard values that agree with published values from other laboratories for Δ_{47} (Bernasconi et al., 2021) and Δ_{48} (Bajnai et al., 2020; Fiebig et al., 2021; Swart et al., 2021).

Briefly, we describe analysis and instrumentation here. For this work, measurements were made between September 2018 and November 2021. The general configuration used for clumped isotope measurements on these two instruments is (1) phosphoric acid digestion of 0.5 mg $CaCO_3$, (2) evolved CO_2 gas purification, and (3) isotopic measurements via the mass spectrometer.

The Nu Perspective IRMS is optimized for clumped isotope analysis with secondary electron suppression, which increases the signal-to-noise ratio. Energy filters and quadratic lenses fitted in front of the Faraday collectors for m/z 47, 48, and 49 drives the suppression. The detectors for m/z 44, 45, and 46 are registered through 3×10^8, 3×10^{10}, and 3×10^{11} Ω resistors, respectively. The detectors for m/z 47, 48, and 49 are registered with 3×10^{12} Ω resistors. A dual-inlet system allows for the input of the sample gas and a reference gas controlled by a bellows system that inputs both gasses through a changeover block, so the sample and reference gases can be compared in real-time. The reference gas and sample gas pressures are precisely matched with continuous pressure adjustments to achieve 24 V on mass 44 at the start of every acquisition block, and the pressure varies between 24 and 9 V during an acquisition block. Data were taken in 3 blocks of 20 cycles, for a total of 60 cycles of sample to standard comparison, with an 8 s changeover delay and 20 s of integration per cycle, for a total integration time of 1200 s.

Nu Perspective-1 and Nu Perspective-2a used an in-house built,

Table 1
Sample information provided by Christensen et al. (2021).

Sample Name	Sample Composition	Location	Notes
A	Travertine	NS1	Wedding Cake – Rim Formation
AA	Aragonite 91%; Calcite 1%; Brucite 8%	BSC	Mixed Water (BSC + Creek)
Alpha	Travertine	BSC	Wedding Cake – Rim Formation
B	Unspecified (Non-Travertine)	New Pool	Mixed Water (New Pool Spring + Creek)
C1	Aragonite 86%; Calcite 7%; Brucite 7%	BSC	Snow – Bottom of Pool
J	Unspecified (Non-Travertine)	GPS	Unspecified
K	Aragonite 25%; Calcite 20%; Hydromagnesite 50%; Nitromagnesite 2%; Nesquehonite 3%	GPS	Snow – Bottom of Pool
L	Unspecified (Non-Travertine)	GPS	Pool Floe
P	Aragonite 78%; Calcite 18%; Brucite 4%	BSC	Pool Floe
PA-C2	Unspecified (Non-Travertine)	BSC	Snow – Bottom of Pool
PB-C1	Aragonite 86%; Calcite 7%; Brucite 7%	BSC	Snow – Bottom of Pool
PB-C2	Aragonite 46%; Calcite 49%; Brucite 5%	BSC	Outer Edge Surface
PE-C2	Aragonite 78%; Calcite 18%; Brucite 4%	BSC	Outer Edge Surface
PE-C3	Unspecified (Non-Travertine)	BSC	Snow – Bottom of Pool
Q	Unspecified (Non-Travertine)	NS1	Wedding Cake – Floe
S	Unspecified (Non-Travertine)	BSC	Mixed Water (BSC + Creek)
T1	Travertine	BSC	Hand Sample – Multiple Layers
T2	Travertine	BSC	Hand Sample – Multiple Layers
T3a	Travertine	BSC	Hand Sample – Multiple Layers
T3b	Travertine	BSC	Hand Sample – Multiple Layers
T4	Travertine	BSC	Hand Sample – Multiple Layers
T5	Travertine	BSC	Hand Sample – Multiple Layers
U	Unspecified (Non-Travertine)	BSC	Pool Floe
V	Unspecified (Non-Travertine)	BSC	Pool Floe
X	Unspecified (Non-Travertine)	BSC	Pool Floe

automated system commonly referred to as the "Autoline," similar to the system from Passey et al. (2010). The autoline consists of (1) a Costech Zero Blank autosampler made of stainless steel that is capable of pulling high vacuum, (2) a common acid bath (CAB) containing 105 wt% phosphoric acid where 1 mg (Nu Perspective-1) or 0.5 mg (Nu Perspective-2a) of $CaCO_3$ is reacted at 90 °C, (3) cryogenic traps (dry ice and ethanol, and liquid nitrogen) for CO_2 purification through removal of water and other gases with low vapor pressures, and collection of CO_2, (4) an in-line elemental-silver wool (Sigma-Aldrich) column to remove sulfur compounds from the gas mixture, (5) a gas chromatograph (GC) column (UHP Helium carrier gas, Porapak Type-Q TM 50/80 mesh column packing material) held at −20 °C during the gas transit to separate CO_2 from the remaining components of the produced gas mixture, and (6) a final cryogenic purification stage before transfer of CO_2 into the bellows of the mass spectrometer.

Nu Perspective-2b uses a Nu Carb Sample Digestion System instead of a CAB, where 0.5 mg of $CaCO_3$ is digested at 70 °C in individual glass vials with 105 wt% phosphoric acid. The sample gas is cryogenically purified in liquid nitrogen-cooled tubes called coldfingers before passing through a relatively short GC column packed with Porapak Type-QTM 50/80 and silver wool. This instrument operates under vacuum pressure and does not use a carrier gas.

2.2.1. Standardization and data processing

Data was processed and corrected using Easotope 64-bit, release version 20201231 (John and Bowen, 2016) with IUPAC parameters (Brand et al., 2010; Daëron et al., 2016). The CO_2 reference gas used to establish real-time comparison to unknown sample compositions was sourced from Oztech and has an isotopic composition as follows: $\delta^{18}O_{VSMOW} = 24.9‰$; $\delta^{13}C_{VPDB} = -3.56‰$. The Δ_{47} values are reported in the Intercarb-Carbon Dioxide Equilibrium Scale (I-CDES) reference frame, meaning they were normalized to nominal carbonate standard values for ETH-1, ETH-2, and ETH-3 determined in Bernasconi et al. (2021), and additional in-house standards with values also determined in the I-CDES reference frame (Upadhyay et al., 2021; Lucarelli et al., 2023). The Δ_{48} values are reported in the Carbon Dioxide Equilibrium Scale (CDES 90) reference frame and normalized to carbonate standards values digested at 90 °C reported in Lucarelli et al. (2023). The standards used in empirical transfer functions (ETFs) for data normalization, using methods detailed in Dennis et al. (2011), include Carmel Chalk, CM Tile (Carrara Marble Tile), ETH-1, ETH-2, ETH-3, ETH-4, and Veinstrom (Upadhyay et al., 2021; Lucarelli et al., 2023). International standards ETH-1 and ETH-2 (Bernasconi et al., 2018, 2021) were used for nonlinearity corrections associated with both Δ_{47} versus δ^{47} and Δ_{48} versus δ^{48} raw data. Both the ETFs and nonlinearity corrections are calculated using a moving average of ±10 standard replicates. The clumped isotope measurement errors are reported as ±1 standard error (SE) and ±1 standard deviation (SD), and the carbon and oxygen isotope measurement errors are given as ±1 SD. All data regressions were determined in PRISM Version 9.5.0 for macOS using the function "simple linear regression", where the slope and intercept error are reported as ±1 SE.

The reproducibility of standard Δ_{47} and Δ_{48} values on each instrument configuration are given in Table S1, and all sample and standard replicate data are reported in Tables S2 and S3, respectively. Figs. S1–S3 show the ETH-1 and ETH-2 values from each correction interval. Fig. S4 shows the standard residual values (measured value – expected value), and Table S4 reports statistical tests (D'Agostino and Pearson test, performed in PRISM) which indicate standard residuals from each instrument configuration were normally distributed. All supplemental tables and information on clumped isotope data quality assurance can be found in the Data Availability statement.

2.3. Modeling of DIC-H_2O-CO_2 system using IsoDIC

To study the time evolution of the HCO_3^- and CO_3^{2-} endmembers in a CO_2 absorption-driven pathway that simulated the conditions of springs at The Cedars, we used the IsoDIC modeling software developed by Guo and Zhou (2019) and Guo (2020). This modeling software simulates reactions (10)–(14), predicting kinetic isotope fractionation in oxygen and clumped isotopes in a DIC-H_2O-CO_2 system from (de)hydration and (de)hydroxylation reactions. The model tracks the isotopologue reactions involving all major isotopes of C and O, for a total of 155 reactions. The forward and reverse rate constants were estimated using Eq. (17),

$$k^* = a_{KIE}{}^*k \tag{17}$$

where k is the rate constant of the isotopically unsubstituted reactions, and a_{KIE} is the kinetic fractionation factor (KFF) for the isotopically substituted reactions. The product of these variables yields k^*, the modified rate constant for the isotopically substituted reactions. (De)hydration and (de)hydroxylation reactions, reactions (10) and (11), are the only reactions that contribute to isotopic fractionation where reactions (12)–(14) are assumed to be at equilibrium due to their relatively

fast reaction rates when compared to reactions (10) and (11) (Guo and Zhou, 2019; Guo, 2020).

Parameters measured *in-situ* for surface floe samples (Samples L, P, U, V, PE-C2, PB-C2, and X) from The Cedars were used to simulate conditions associated with The Cedars Springs (Morrill et al., 2013). The following parameters were input into the IsoDIC software to perform modeling in the CO_2 absorption regime: (1) solution temperature = 17.5 °C, (2) solution pH = 11.5, (3) air pCO_2 = 400 ppm, (4) $\delta^{13}C_{VPDB}$ of air = −8.431‰, and (5) $\delta^{18}O_{VPDB}$ of water = −36.3 ± 0.6‰, taken as the average of measurements from the NS1, GSP1, and BSC locations (Morrill et al., 2013). The system evolution time parameter was set to 1, 10, 50, 100, and 1000 h to simulate different timescales for the evolution of the HCO_3^- and CO_3^{2-} DIC species. We note that modern samples were collected from locations where surface creek (pH = 8.7) and spring waters (pH = 11.5) are mixing, resulting in a potential drop in pH to an intermediate value (pH = 8.7–11.5) that would reduce equilibration times from the longer values associated with highly alkaline solutions. The equations used by this model are described in the Supplementary Material S.1.

The conversion of carbonate minerals into gaseous CO_2 is associated with a temperature-dependent preferential removal of ^{16}O relative to ^{18}O and is corrected by an acid fractionation factor (AFF), denoted by y in Eqs. (18) and (19) (Guo et al., 2009).

$$\Delta_{47} = \Delta_{63} + y \tag{18}$$

$$\Delta_{48} = \Delta_{64} + y \tag{19}$$

An AFF is applied to measured Δ_{47} and Δ_{48} values for comparison to modeled Δ_{63} and Δ_{64} values. The reference frame and temperature to which the value is being converted also dictates the value of y. An AFF of $y = 0.196‰$ was used in the conversion between Δ_{63} and Δ_{47} values, and an AFF of $y = 0.131‰$ was used in the conversion between Δ_{64} and Δ_{48} values (Lucarelli et al., 2023).

2.4. Modeling of the $CaCO_3$-DIC-H_2O system using COAD

To model the KIEs in the clumped and stable isotope data of the carbonate minerals with respect to the conditions at The Cedars, we used the COAD (Carbon, Oxygen, α, Δ) model (Watkins and Devriendt, 2022), which builds upon the ExClump38 model (Chen et al., 2018; Uchikawa et al., 2021) by including the mineral precipitation reactions and growth rates (Watkins and Hunt, 2015). Mineral growth rates are important for two reasons. First, it has been hypothesized the KIEs attending these reactions can lead to differences between the clumped isotope composition of the solid phase relative to DIC (Tripati et al., 2015). Second, the mineral growth rates affect the reversibility of the hydration and hydroxylation reactions such that fast growth rates pull these reactions closer to the kinetic limit (Watkins and Devriendt, 2022).

For comparison between outputs from COAD and IsoDIC, we used the same KFFs and model input parameters for isotopic values, temperature, and pH in our calculations (see the previous section). The COAD model involves a total of 17 differential equations to model reactions (10)–(16), which track the evolution of the $\delta^{18}O$, $\delta^{13}C$, Δ_{47}, and Δ_{48} values of DIC species in solution and the precipitating $CaCO_3$ (Watkins and Hunt, 2015; Watkins and Devriendt, 2022). The rate constants associated with precipitation reactions (15) and (16) are mass-dependent, and the flux of precipitated $CaCO_3$ is controlled by the $[Ca^{2+}]$ and $[CO_3^{2-}]$ (Watkins and Hunt, 2015). In contrast to the IsoDIC model, this model only describes the most abundant isotopologues for the respective masses, while IsoDIC describes all isotopologues in the DIC-H_2O system. The COAD model was also used to calculate the steady-state isotopic values as a function of mineral precipitation rate (R_p). A description of the equations and parameters used are reported in the Supplementary Material S.2. The code used is available for download in the Data Availability Statement.

2.5. Estimation of CO_2 sequestered at the Cedars

Due to the similarity in rock composition and water pH in the Samail Oman and The Cedars peridotite and associated springs (Kelemen and Matter, 2008; Morrill et al., 2013; Christensen et al., 2021), we estimated the rate and amount of CO_2 that could naturally be sequestered at The Cedars based on an approach used in previous work from Kelemen and Matter (2008) for a peridotite body in Oman. Kelemen and Matter (2008) estimated that in the Omani ophiolite, the travertines and carbonate veins comprised a volume of roughly 5.5×10^7 m^3, or a minimum of $\approx 10^{11}$ kg of CO_2. In addition, for the determination of rates of carbonation for the two different types of waters (Fig. 1), they make two key assumptions. First, in Type 1 waters, they assume the complete consumption of DIC to precipitate carbonate minerals as Type 2 waters are formed. Second, they assume that differences in dissolved Ca^{2+} between the two types of waters leads to calcite precipitation as Type 2 waters reach the surface. Using this approach, they calculated that carbonate mineralization in the region consumes $\sim 4 \times 10^7$ kg of atmospheric CO_2 per year, or ≈2 tons/km^3/year of peridotite.

We estimated the total sequestration potential at The Cedars. For this calculation, we summed the amount of CO_2 that would be consumed if the total amount of Mg, Ca, and Fe in relict olivine was consumed by carbonation. We assumed that The Cedars peridotite is composed of 70% olivine which is 43.82 wt% Mg, 5.34 wt% Fe, and 0.52 wt% Ca (Coleman, 2000; Blake et al., 2012; Morrill et al., 2013), has a volume of 44.8 km^3 (Coleman, 2000), a density of partially serpentinized peridotite of 2800 kg/m^3 (Carnevale, 2013), total mass of 1.25×10^{14} kg (calculated from the volume and density), and a carbonation rate of 1% (Kelemen and Matter, 2008). Below, we show how this calculation was performed for Mg.

$$(1.25 \times 10^{14}\ \text{kg}) \times 0.70 \times 0.4382 \times 0.01 \times \frac{CO_2\ \ 44\ \ g/mol}{Mg\ \ 24.3\ \ g/mol} = 7.0 \times 10^{11}$$

kg CO_2 sequestered.

We used the conservative estimate of calcite growth rate in The Cedars springs of 4.8×10^7 mol/m^2/s (Christensen et al., 2021) to estimate the rate of CO_2 sequestered in the springs per year.

For comparison, we report a set of calculations for the CRO from Carnevale (2013) that also utilize the methods of Kelemen and Matter (2008). To estimate the amount of CO_2 sequestered in the CRO per year, we used the CO_2 sequestration potential reported in Carnevale (2013) and the natural carbonation rate for peridotite determined in Kelemen and Matter (2008).

Additionally, Kelemen and Matter (2008) assumed the natural rates of CO_2 uptake could be enhanced by $\sim 10^6$ times by drilling and hydraulic fracturing of the rock to increase the reactive surface area, initial heating of the rock to 185 °C using hot fluids, followed by the injection of CO_2 (pressure = 300 bars, temperature = 25 °C, flow rate = 0.040 m/s). They estimate this would result in a sequestration rate of $\sim 2 \times 10^9$ tons of CO_2 sequestered per km^3. This rate was used to estimate the time elapsed before all peridotite would be converted into carbonate minerals from enhanced *in situ* carbonation at The Cedars, CRO, and Oman ophiolite. The parameters used in all calculations are reported in Table S5.

3. Results

3.1. Dual clumped isotope analysis

Dual clumped isotope values (Δ_{47}, Δ_{48}) are reported for samples from The Cedars in Fig. 3 and Table 2. The Δ_{47} and Δ_{48} values range from 0.595‰ to 0.791‰ and −0.506‰ to 0.282‰, respectively. The samples that are within error (±1 SE) of an equilibrium regression (Lucarelli et al., 2023) are A, AA, B, and J. All other samples exhibit apparent KIEs, with the greatest departure from equilibrium in sample V (Δ_{47} = 0.779‰; Δ_{48} = −0.506‰; Fig. 3). The sampling location of each

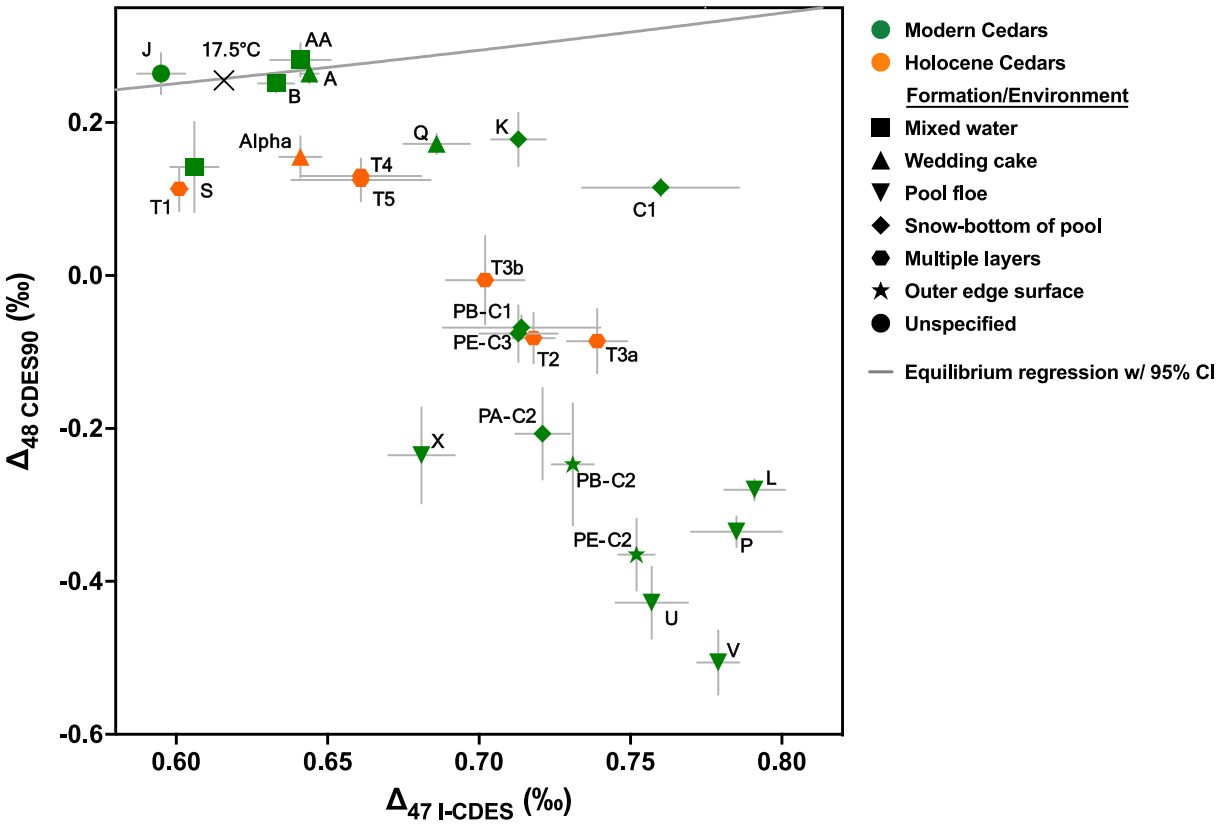

Fig. 3. The Δ_{47} and Δ_{48} values for modern (green symbols) and Holocene (orange symbols) carbonate mineral samples from The Cedars. Results are compared to equilibrium values (gray line) (Lucarelli et al., 2023), with the average water temperature at The Cedars of 17.5 ± 1 °C (Morrill et al., 2013; Christensen et al., 2021) indicated (X symbol). The samples that exhibit the largest KIEs were primarily recovered from surface floes (pool floe, downward triangles). The samples that are within error (±1 SE) of equilibrium are from areas where surface and spring waters mix (squares), 1 wedding cake sample (triangle), and 1 sample from the GPS location from an unspecified formation (circle). A linear regression through all samples indicates a slope of −3.223 ± 0.519. Error bars indicate ± 1 SE.

Table 2
Clumped and bulk isotopic values for all samples measured in this study. The calculations to determine $\Delta\delta^{18}O$, $\Delta\Delta_{47}$, and $\Delta\Delta_{48}$ values were performed assuming equilibrium values for the average temperature at The Cedars of 17.5 °C (Kim et al., 2007; Dietzel et al., 2009; Morrill et al., 2013; Christensen et al., 2021; Lucarelli et al., 2023).

Sample Name	Number of Replicates	$\delta^{13}C_{VPDB}$ (‰)	1 S.D.	$\delta^{18}O_{VPDB}$ (‰)	1 S.D.	$\Delta\delta^{18}O$ (‰)	$\Delta_{47\ I\text{-}CDES}$ (‰)	1 S.D.	1 S.E.	$\Delta\Delta_{47}$ (‰)	$\Delta_{48\ CDES90}$ (‰)	1 S.D.	1 S.E.	$\Delta\Delta_{48}$ (‰)
A	3	−14.1	0.0	−3.6	0.1	3.8	0.644	0.005	0.003	0.028	0.264	0.022	0.013	0.009
AA	6	−12.4	0.1	−3.0	0.1	3.6	0.641	0.024	0.010	0.025	0.282	0.054	0.022	0.027
Alpha	6	−9.6	0.1	−2.8	0.1	4.5	0.641	0.016	0.007	0.025	0.155	0.066	0.027	−0.100
B	3	−12.0	0.0	−3.7	0.0	3.6	0.633	0.010	0.006	0.017	0.251	0.021	0.012	−0.004
C1	4	−16.1	0.1	−7.8	0.2	−1.2	0.760	0.051	0.026	0.144	0.115	0.025	0.012	−0.140
J	4	−13.2	0.0	−0.1	0.2	7.2	0.595	0.015	0.008	−0.021	0.264	0.054	0.027	0.009
K	9	−15.3	0.8	−6.9	0.8	0.4	0.713	0.027	0.009	0.097	0.178	0.104	0.035	−0.077
L	4	−23.4	0.1	−15.1	0.1	−7.8	0.791	0.020	0.010	0.175	−0.280	0.027	0.014	−0.535
P	5	−27.3	0.0	−19.3	0.0	−12.7	0.785	0.033	0.015	0.169	−0.335	0.045	0.020	−0.590
PA-C2	5	−20.0	0.1	−10.7	0.2	−3.4	0.721	0.020	0.009	0.105	−0.207	0.134	0.060	−0.462
PB-C1	3	−17.4	0.0	−8.6	0.1	−2.0	0.714	0.045	0.026	0.098	−0.068	0.028	0.016	−0.323
PB-C2	5	−20.5	0.5	−12.7	0.8	−5.4	0.731	0.016	0.007	0.115	−0.247	0.180	0.080	−0.502
PE-C2	11	−22.1	0.2	−14.7	0.4	−8.1	0.752	0.021	0.006	0.136	−0.365	0.157	0.047	−0.620
PE-C3	8	−16.2	0.2	−8.1	0.3	−0.8	0.713	0.035	0.013	0.097	−0.076	0.105	0.037	−0.331
Q	5	−17.6	0.1	−6.7	0.1	0.7	0.686	0.025	0.011	0.070	0.172	0.029	0.013	−0.083
S	3	−11.7	0.0	−2.7	0.1	4.6	0.606	0.014	0.008	−0.010	0.142	0.102	0.059	−0.113
T1	6	−9.8	0.1	−3.2	0.2	4.1	0.601	0.007	0.003	−0.015	0.113	0.072	0.029	−0.142
T2	13	−14.6	0.2	−9.6	0.3	−2.3	0.718	0.024	0.007	0.102	−0.082	0.119	0.033	−0.337
T3a	13	−15.0	0.4	−9.4	0.4	−2.0	0.739	0.036	0.010	0.123	−0.086	0.153	0.042	−0.341
T3b	3	−13.7	0.2	−7.8	0.1	−0.5	0.702	0.023	0.013	0.086	−0.006	0.100	0.058	−0.261
T4	3	−10.0	0.1	−3.5	0.1	3.8	0.661	0.039	0.023	0.045	0.125	0.049	0.028	−0.130
T5	3	−9.2	0.0	−3.1	0.0	4.3	0.661	0.035	0.020	0.045	0.130	0.013	0.007	−0.125
U	5	−26.6	0.0	−18.7	0.1	−11.4	0.757	0.028	0.012	0.141	−0.428	0.104	0.047	−0.683
V	11	−23.7	0.1	−14.8	0.1	−7.5	0.779	0.023	0.007	0.163	−0.506	0.139	0.042	−0.761
X	7	−22.4	0.1	−15.4	0.1	−8.1	0.681	0.029	0.011	0.065	−0.235	0.167	0.063	−0.490

sample can be seen in Fig. 2. A linear regression of the Δ_{48}-Δ_{47} values from The Cedars yields a slope of −3.223 ± 0.519.

3.2. Clumped and stable isotopes

The $\delta^{18}O$ and $\delta^{13}C$ values for The Cedars samples range from −19.3‰ to −0.1‰ and −27.3‰ to −9.2‰, respectively (Table 2). The Δ_{47} of modern and Holocene samples from The Cedars are plotted versus $\delta^{18}O$ and $\delta^{13}C$ and compared to samples from alkaline springs in the Oman ophiolite (Falk et al., 2016) (Fig. 4A, C). The measured values from The Cedars and Oman are also compared to calculated equilibrium values. The calculated equilibrium $\delta^{18}O_{CaCO3}$ (VPDB) range was determined to be −8.2‰ to −6.6‰ for calcite and aragonite (Kim and O'Neil, 1997; Kim et al., 2007; Dietzel et al., 2009), given The Cedars $\delta^{18}O_{water}$ value of −36.3 ± 0.6‰ (VPDB), taken as the average of measurements from the NS1, GSP1, and BSC locations (Morrill et al., 2013). The equilibrium Δ_{47} value (Lucarelli et al., 2023) for the average water temperature of 17.5 ± 1 °C (Christensen et al., 2021; Morrill et al., 2013) was determined to be 0.616 ± 0.003‰. All samples show departures from equilibrium oxygen isotope values.

Linear regressions through The Cedars and Oman datasets are in strong agreement. The $\Delta_{47}/\delta^{18}O$ and $\Delta_{47}/\delta^{13}C$ data regressions for The Cedars samples both exhibit slopes of −0.009 ± 0.001 (Fig. 4A, C). The $\Delta_{47}/\delta^{18}O$ and $\Delta_{47}/\delta^{13}C$ data regressions for the Oman samples (Falk et al., 2016) exhibit slopes of −0.006 ± 0.002 and −0.005 ± 0.002, respectively. When The Cedars and Oman datasets are combined, the slopes of the $\Delta_{47}/\delta^{18}O$ and $\Delta_{47}/\delta^{13}C$ data regressions are −0.007 ± 0.001 and −0.006 ± 0.001, respectively.

The Δ_{48} versus $\delta^{18}O$ and $\delta^{13}C$ values for The Cedars are also reported (Fig. 4B, D; Table 2), and compared to equilibrium. The equilibrium Δ_{48} value (Lucarelli et al., 2023) for the average water temperature of 17.5 ± 1 °C (Morrill et al., 2013; Christensen et al., 2021) was determined to be 0.255 ± 0.002‰. The $\Delta_{48}/\delta^{18}O$ and $\Delta_{48}/\delta^{13}C$ regression slopes are 0.041 ± 0.003 and 0.038 ± 0.005, respectively.

3.3. Clumped and oxygen isotope disequilibrium

The extent of clumped and oxygen isotope disequilibrium ($\Delta\Delta_{47}$, $\Delta\Delta_{48}$, and $\Delta\delta^{18}O$) in The Cedars was calculated by taking the difference between the measured values and calculated equilibrium values (Kim and O'Neil, 1997; Kim et al., 2007; Dietzel et al., 2009; Lucarelli et al., 2023) (Table 2). The $\Delta\Delta_{47}$, $\Delta\Delta_{48}$, and $\Delta\delta^{18}O$ values are compared to theoretical slopes determined by Guo (2020) for various kinetic processes (Fig. 5). The $\Delta\delta^{18}O$ values range from −12.7‰ to 7.2‰, while $\Delta\Delta_{47}$ and $\Delta\Delta_{48}$ values range from −0.021‰ to 0.175‰ and −0.761‰ to 0.027‰, respectively (Table 2). The slopes of the $\Delta\Delta_{47}/\Delta\delta^{18}O$, $\Delta\Delta_{48}/\Delta\delta^{18}O$, and $\Delta\Delta_{48}/\Delta\Delta_{47}$ are −0.009 ± 0.001, 0.040 ± 0.003, and −3.223 ± 0.519, respectively.

3.4. Modeled clumped isotope evolution

Measured Δ_{47} and Δ_{48} values for The Cedars samples were compared to IsoDIC (Guo, 2020) model predictions for the time-dependent isotopic evolution of HCO_3^- and CO_3^{2-} (Fig. 6A). The measured values are consistent with the range of Δ_{47} and Δ_{48} values predicted by the model for HCO_3^- and CO_3^{2-}. The measured Δ_{47} and Δ_{48} values were also compared to model predictions for $CaCO_3$, HCO_3^-, CO_3^{2-}, and equilibrated inorganic carbon (EIC) using the COAD model (Watkins and Devriendt, 2022) (Fig. 6B–D). Measured $\delta^{18}O$ and Δ_{47} values are largely consistent with model predicted values, however, the Δ_{48} values for the ancient travertine samples and snow samples collected from the bottom of the pool (Table 1) were offset from the COAD model predicted values for $CaCO_3$ by up to 0.1‰ (Fig. 6D).

The average Δ_{47} and Δ_{48} values and growth rate for samples with relatively large KIEs that were collected at the BSC springs location (samples U, V, X; Fig. 2) were compared to COAD model predictions for the evolution of clumped isotope values for calcite with a varying precipitation rate (Fig. 6E, F). The model accurately predicted the measured Δ_{47} value of 0.744 ± 0.010‰ within 1 SE, while the measured Δ_{48} value of −0.407 ± 0.037‰ was offset from the model predicted value of −0.264‰ by −0.143‰.

3.5. CO_2 sequestration

We estimate the peridotite body at The Cedars could sequester a maximum of ~7.4 × 10^8 tons of CO_2 at a natural rate of ~63 tons/year. It would take ~3.7 × 10^8 years to reach the maximum amount of sequestration (Fig. 7). The Cedars springs could sequester an additional ~370 tons/year. If we utilize estimates of the volume and total sequestration potential of the CRO (Carnevale, 2013), we estimate that ~1.1 × 10^4 tons of CO_2 could be naturally sequestered per year at the CRO, with the maximum CO_2 sequestration potential achieved after ~4.9 × 10^{10} years. If the enhanced *in situ* carbonation rate of ~2 × 10^9 tons CO_2/km^3/year described in Kelemen and Matter (2008) were used, all olivine in the CRO could be converted into carbonate minerals in <50 years.

4. Discussion

4.1. Broad patterns in multi-isotope space: Comparison of sample sets

The similarity in $\Delta_{47}/\delta^{18}O$ and $\Delta_{47}/\delta^{13}C$ regression slopes for The Cedars data and data from surface springs and veins in the Samail ophiolite of Oman (Falk et al., 2016) (Fig. 4A, C) suggest the same processes are driving disequilibrium in both systems. However, regional, and possible local and temporal, variations in the $\delta^{18}O$ of waters, and $\delta^{13}C$ of DIC, also are reflected in these data. For example, the Oman dataset (Falk et al., 2016) may have larger fluctuations in $\delta^{13}C$ and $\delta^{18}O$ due to the amount and type of samples analyzed, and greater fluctuations in DIC $\delta^{13}C$ and meteoric water $\delta^{18}O$ due to the significantly larger area, 200 km × 50 km, of the Oman site (Christensen et al., 2021). In contrast, the Δ_{47}-Δ_{48} dual clumped isotope approach allows for mechanistic fingerprinting of the processes associated with disequilibria, and a rough estimation of timescales for equilibration. This represents a major advancement in the clumped isotope field as data from different localities, natural and synthetic, can be directly compared for potential sources of disequilibrium. An additional benefit of clumped isotopes is the method can be used without knowledge of additional parameters such as the isotopic composition of the parent fluid or DIC source.

The majority of Cedars samples exhibit an enrichment in Δ_{47} accompanied by a depletion in Δ_{48}, with a $\Delta\Delta_{48}/\Delta\Delta_{47}$ slope of −3.223 ± 0.519. Our observed slope is intermediate between the theoretically calculated slopes for KIEs from CO_2 hydration and hydroxylation reactions during CO_2 absorption (25 °C; pH 9) and in high pH travertine (28 °C; pH 11.5), which have slopes of −1.72 and −8.33, respectively (Guo, 2020) (Fig. 5). Thus, the disequilibria at The Cedars and Oman are occurring through a similar pathway that is largely associated with CO_2 hydroxylation. We note a similar trend was also reported by Bajnai et al. (2020) in their dual-clumped investigation of cold-water coral, warm-water coral, and brachiopods, and in a cold-water coral sample reported by Lucarelli et al. (2023). Both studies concluded hydration/hydroxylation during CO_2 absorption drove kinetic biases in the dual clumped isotope values.

4.2. (Dis)equilibrium within the Cedars depends on sample location

Sample location within The Cedars was a major factor influencing whether bulk and clumped isotopic data exhibited departures from equilibria, likely linked to variations in DIC sources (i.e., Type 1 and Type 2 waters) and equilibration time. Modern samples L, P, U, V, PB-C2, and PE-C2 collected from surface pool floes located at the BSC and GPS locations (Fig. 2) exhibited the greatest KIEs (Figs. 3–6). At these

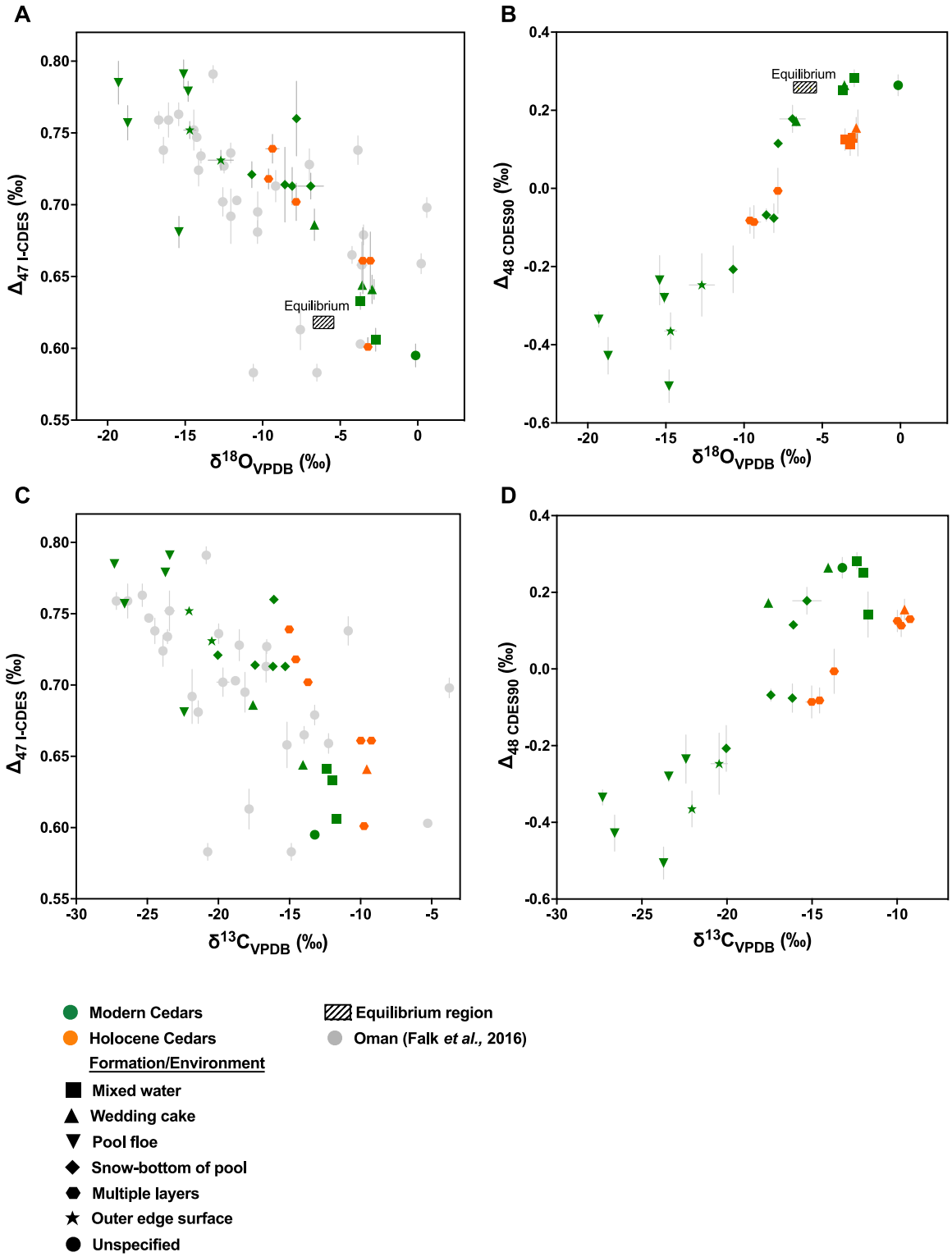

Fig. 4. Clumped isotope (Δ_{47}, Δ_{48}) versus bulk isotope ($\delta^{18}O$, $\delta^{13}C$) results of modern (green symbols) and Holocene (orange symbols) surface spring carbonate samples from The Cedars. Results are compared to calculated equilibrium values (striped rectangle) (Kim and O'Neil, 1997; Kim et al., 2007; Dietzel et al., 2009; Lucarelli et al., 2023). Panels A and C include data from carbonate veins precipitated from a peridotite body in Oman (gray cirlces) (Falk et al., 2016). (A) Δ_{47} versus $\delta^{18}O$ values for The Cedars and Oman. A linear regression fit to The Cedars values yields a slope of -0.009 ± 0.001, and a linear regression for the Cedars and Oman values yields a slope of -0.007 ± 0.001. (B) Δ_{48} versus $\delta^{18}O$ values for The Cedars. A linear regression fit to The Cedars values yields a slope of 0.041 ± 0.003. (C) Δ_{47} versus $\delta^{13}C$ values for The Cedars and Oman (Falk et al., 2016). A linear regression fit to The Cedars values yields a slope of -0.009 ± 0.001, and a linear regression fit to The Cedars and Oman values yields a slope of -0.006 ± 0.001. (D) The Δ_{48} versus $\delta^{13}C$ values for The Cedars. A linear regression yields a slope of 0.038 ± 0.005. The Oman Δ_{47} values were published in the CDES 25 reference frame and converted to the CDES 90 reference frame (which is comparable to the I-CDES reference frame used here) using an acid fractionation factor of 0.092‰ (Henkes et al., 2013). Equilibrium values were calculated using the average water temperature at The Cedars of 17.5 °C (Morrill et al., 2013; Christensen et al., 2021). Error bars indicate ± 1 SE for clumped isotope values and ± 1 SD for bulk isotope values.

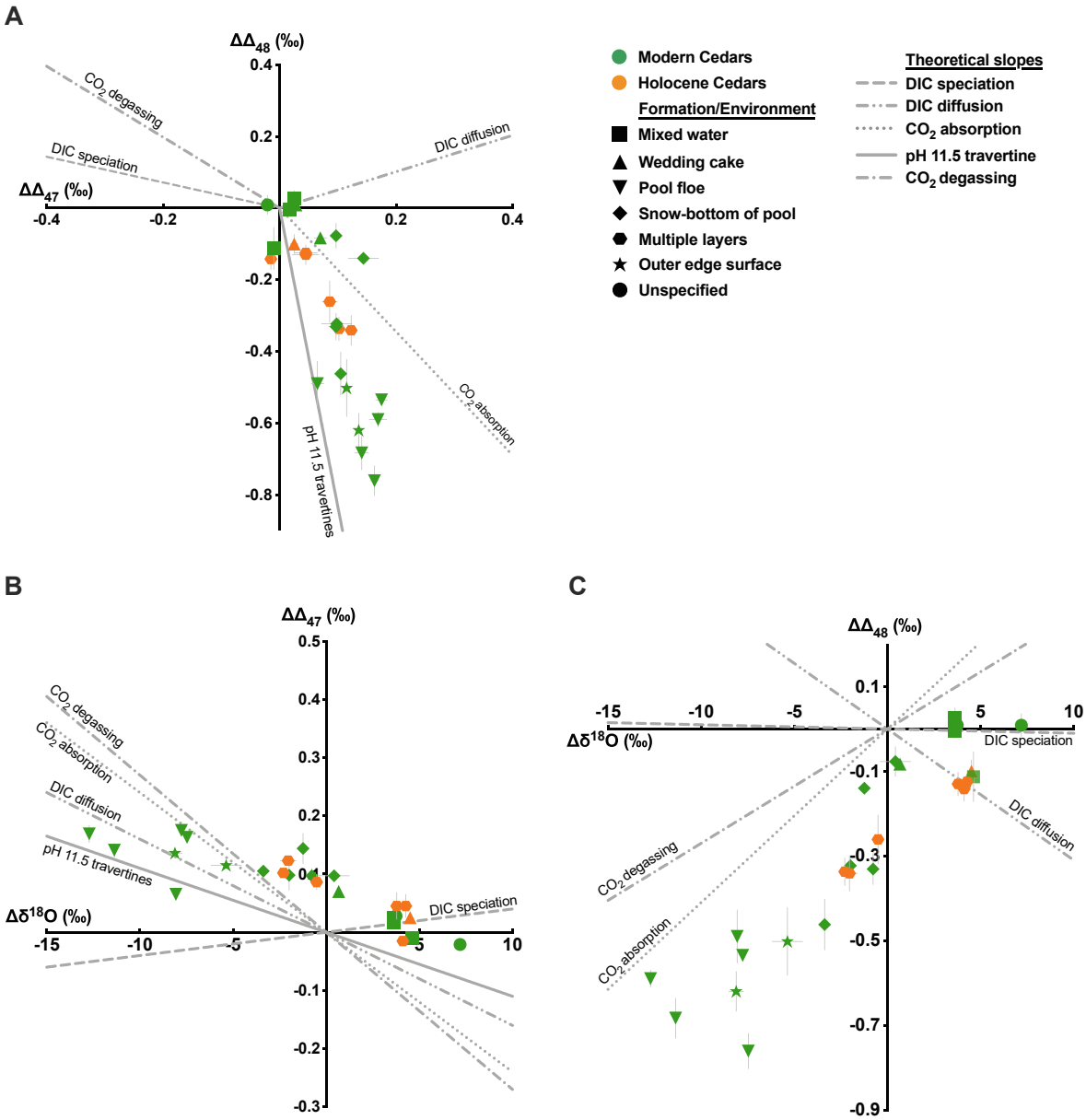

Fig. 5. Extent of disequilibria in clumped (Δ_{47} and Δ_{48}) and oxygen isotope ($\delta^{18}O$) values in the modern (green symbols) and Holocene (orange symbols) Cedars samples are shown with theoretically predicted kinetic slopes from multiple processes (gray lines) (Guo, 2020). The $\Delta\Delta_{47}$, $\Delta\Delta_{48}$, and $\Delta\delta^{18}O$ values were calculated by taking the difference between the measured values and the calculated equilibrium values (Kim and O'Neil, 1997; Kim et al., 2007; Lucarelli et al., 2023) for the average water temperature of The Cedars of 17.5 °C (Morrill et al., 2013; Christensen et al., 2021). (A) $\Delta\Delta_{48}$ versus $\Delta\Delta_{47}$ values, with a linear regression slope of -3.223 ± 0.519. (B) $\Delta\Delta_{47}$ versus $\Delta\delta^{18}O$ values, with a linear regression slope of -0.009 ± 0.001. (C) $\Delta\Delta_{48}$ versus $\Delta\delta^{18}O$ values, with a linear regression slope of 0.040 ± 0.003. Error bars indicate ±1 SE for clumped isotope values and ±1 SD for $\delta^{18}O$ values.

two localities, KIEs could be related to the rapid uptake of CO_2 at the surface, leading to similarly rapid carbonate mineral precipitation at the air and water interface. These results would be consistent with the interpretations of bulk stable isotopic data by Christensen et al. (2021), who investigated the dynamics associated with $CaCO_3$ precipitation and stable isotope fractionation in surface floes, and argued that at The Cedars, KIEs may be the largest when $CaCO_3$ precipitates at the surface of the springs. The BSC location had a high saturation state (Ω) value of ~13, while the GPS location had an Ω value of ~5. The $[CO_2]$ of the surface layer at the BSC location was calculated to be 1.6×10^{-5} mol/kg-solution, several orders of magnitude higher than the concentration of the bulk pool. The rate of Ca^{2+} replenishment from the springs at the BSC was determined to be 1.5×10^{-6} mol/s, which is comparable to the DIC flux from the atmosphere. The CO_2 from the atmosphere is converted to HCO_3^- via hydroxylation (reaction (11)), with rapid and near-quantitative conversion to CO_3^{2-} (Tripati et al., 2015). With this higher influx of CO_2 and precipitation of $CaCO_3$, the surface pH is reduced slightly from 11.5 in the bulk pool springs to 11.0 at the surface (Christensen et al., 2021). However, the pH is still high enough to favor CO_3^{2-} DIC speciation (Uchikawa and Zeebe, 2012; Tripati et al., 2015) preventing isotopic equilibrium through exchange reactions associated with the other DIC species. In addition, because the concentration of DIC is so high at the surface due to the large CO_2 gradient between the water and atmosphere, the supersaturation state of $CaCO_3$ is also considerably high, further promoting rapid precipitation of $CaCO_3$ outside of isotopic equilibrium (Christensen et al., 2021).

The modern "snow" samples C1, K, PA-C2, PE-C3 and PB-C1 exhibited KIEs that were intermediate between equilibrium and pool

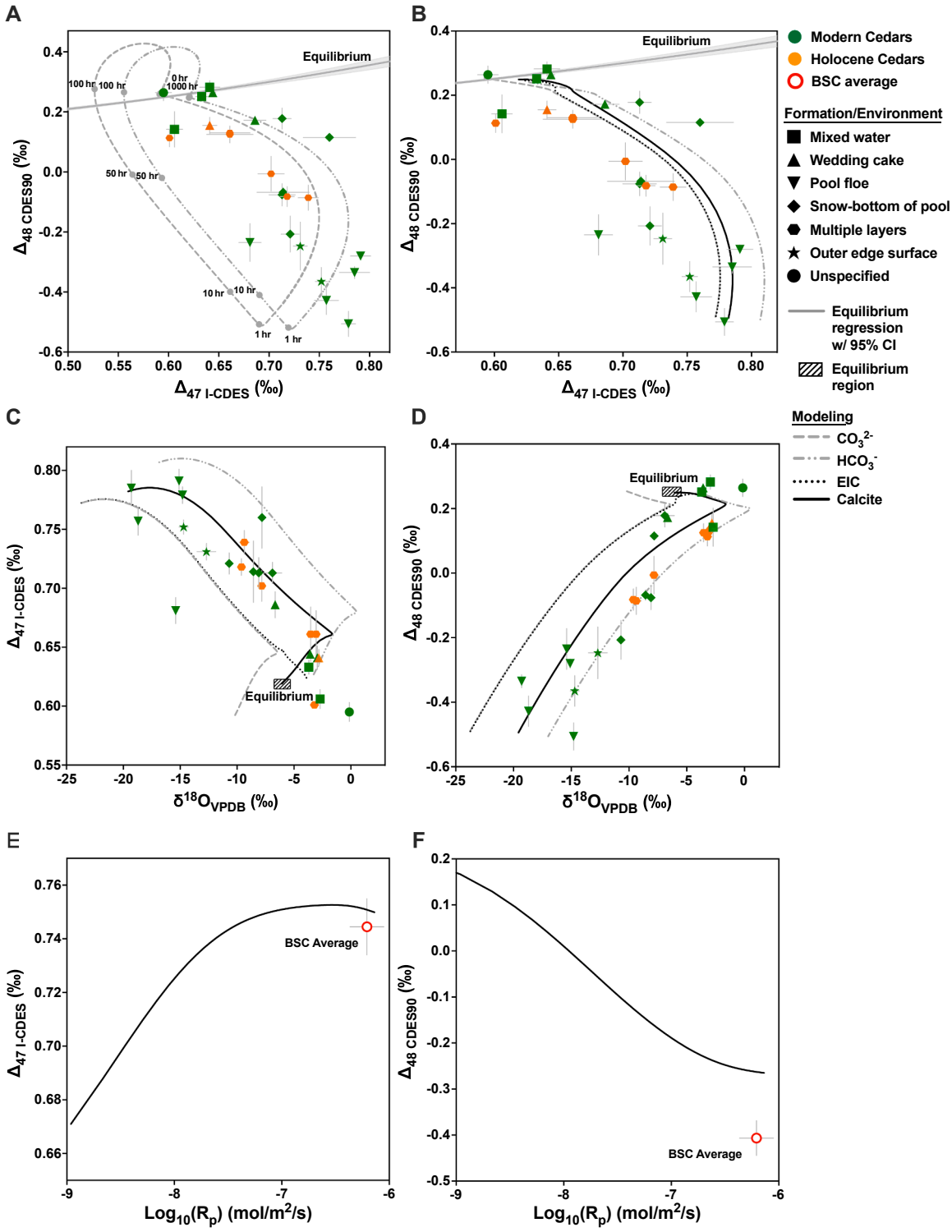

Fig. 6. Measured Δ_{47}, Δ_{48}, and $\delta^{18}O$ values from the modern (green symbols) and Holocene (orange symbols) Cedars samples compared to model predictions (gray and black curves), which were determined using code from the IsoDIC and COAD models. Also shown are the calculated equilibrium values based on the average water temperature at The Cedars of 17.5 °C (gray line in panels A and B; striped rectangle in panels C and D) (Kim and O'Neil, 1997; Kim et al., 2007; Morrill et al., 2013; Christensen et al., 2021; Lucarelli et al., 2023). Panels E and F show the combined average Δ_{47} and Δ_{48} values (red circles) from samples collected at the BSC locality (samples X, U, V), with an apparent growth rate (R_p) of 4.8×10^{-7} to 8.0×10^{-7} mol m^{-2} s^{-1} (Christensen et al., 2021), compared to COAD model predicted values (black curves). (A) Measured Δ_{47} and Δ_{48} values compared to IsoDIC model predicted values for HCO_3^- and CO_3^{-2} with the evolution time indicated. (B) Measured Δ_{47} and Δ_{48} values with COAD model predicted values for calcite, HCO_3^-, CO_3^{-2}, and EIC. (C) Measured Δ_{47} and $\delta^{18}O$ values with COAD model predicted values for calcite, HCO_3^-, CO_3^{-2}, and EIC. (D) Measured Δ_{48} and $\delta^{18}O$ values with COAD model predicted values for calcite, HCO_3^-, CO_3^{-2}, and EIC. (E) The measured and modeled Δ_{47} and $Log_{10}(R_p)$ values. The BSC average Δ_{47} value was determined to be 0.744 ± 0.010‰. (F) Measured and modeled Δ_{48} and $Log_{10}(R_p)$ values. The BSC average Δ_{48} value was determined to be −0.407 ± 0.037‰. The IsoDIC and COAD models were based on the modern Cedars surface floe conditions. Error bars indicate ± 1 SE for clumped isotope values and ± 1 SD for $\delta^{18}O$ values.

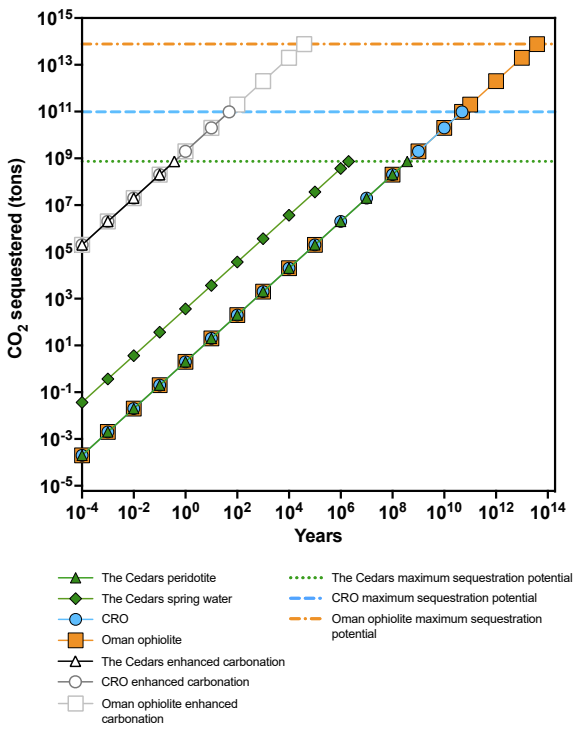

Fig. 7. Calculations of natural rates of CO_2 sequestration in The Cedars peridotite (green triangles), spring water at the site (green diamonds), the Coastal Range Ophiolite (CRO; blue circles), and the Oman ophiolite (orange squares). The estimated maximum CO_2 sequestration potential was calculated to be ~7.4 × 10^8 tons for The Cedars (green dotted line), ~9.7 × 10^{10} tons for the CRO (Carnevale, 2013; blue dashed line), and ~7.7 × 10^{13} tons for the Oman ophiolite (Kelemen and Matter, 2008; orange dash-dot line). The rate of mineral formation in The Cedars springs was measured by Christensen et al. (2021) and constrained here with our dual clumped isotope measurements and modeled carbonate mineralization rates. In addition, the CO_2 sequestered from enhanced *in situ* sequestration is shown for The Cedars (black triangles), CRO (dark gray circles), and the Oman ophiolite (light gray squares), following methods from Kelemen and Matter (2008) for enhanced geologic CO_2 sequestration in the Oman ophiolite of ~2 × 10^9 tons CO_2/km^3/year. For natural carbonation, we estimate that the sequestration potentials at The Cedars, CRO, and Oman ophiolite would be reached after ~3.7 × 10^8 years, ~4.9 × 10^{10} years, and ~3.9 × 10^{13} years, respectively. For enhanced *in situ* carbonation, the maximum sequestration potential at The Cedars, CRO, and Oman Ophiolite could be reached in ~0.37, ~49, and ~39,000 years, respectively. All calculated rates assume complete consumption of Mg, Ca, and Fe in the respective formations (Kelemen and Matter, 2008; Matter and Kelemen, 2009; Carnevale, 2013), and consider the ophiolite in Oman and the CRO to be ~30% relict olivine (Kelemen and Matter, 2008; Carnevale, 2013). The peridotite in The Cedars is ~70% relict olivine (Coleman, 2000; Blake et al., 2012; Morrill et al., 2013).

floe samples (Fig. 3). The term snow is used to describe the physical appearance of fine particulates of $CaCO_3$ aggregating at the bottom of the pools, however, their texture is similar to surface floe samples (Christensen et al., 2021). The thin-film model (Christensen et al., 2021) for surface dynamics suggests that as the surface floes thicken or are perturbed by falling debris, $CaCO_3$ aggregates detach and sink deeper into the springs. The floes would carry some surface waters with the particles (Christensen et al., 2021), and thus could mix in a pool of DIC that is not in isotopic equilibrium, driving KIEs in the clumped and bulk isotope signatures. Even though these detached layers, composed of a mixture of particle aggregates and solution, have moved away from the surface where the majority of rapid precipitation is occurring, isotopic equilibration of DIC within the detached layer is still hindered by the high pH of 11.5 (Beck et al., 2005), which favors hydroxylation and CO_3^{2-} as the most abundant DIC species (Tripati et al., 2015). Given water temperatures, DIC in this fragmented layer can retain its kinetic signature for tens of days at a pH of 11.5 (Usdowski et al., 1991; Beck et al., 2005) which can contribute to the KIEs in dual clumped and bulk isotopes. DIC mixing can also drive deviations from equilibrium in Δ_{47} values (Defliese and Lohmann, 2015).

Modern samples A, AA, B, and J fell within 1 SE of clumped isotope equilibrium (Fig. 3). They were collected where fresh creek water mixed with spring water at the New Pool and BSC localities, where the pH and the influx of Ca^{2+} are reduced, leading to potentially more favorable conditions for isotopic equilibration in the DIC-H_2O-CO_2 system. These samples reflect the composition of isotopically equilibrated DIC from the creek or surface water (pH 7.8–8.7) that occasionally mixes with the high-pH springs (Christensen et al., 2021). The Δ_{47}-reconstructed temperature for the near equilibrium samples is 13.9 ± 3.8 °C and 14.2 ± 3.5 °C, using calibrations from Lucarelli et al. (2023) and Anderson et al. (2021), respectively. These reconstructed temperatures are within error (1 SD) of the average yearly temperature at The Cedars of 17.5 ± 1 °C (Morrill et al., 2013; Christensen et al., 2021).

Ancient travertine samples collected from rim formations at the NS1 locality (Alpha, T1, T2, T3a, T3b, T4, and T5) display a range of disequilibrium values (Figs. 3–6). This range could be due to post-depositional events such as recrystallization in the presence of surface and groundwater mixing, which could have shifted disequilibrium isotopic values towards equilibrium in samples T1, T4, and T5. This would be analogous to what Falk et al. (2016) hypothesized occurred in Oman, where the absence of aragonite in travertine samples may have indicated post-depositional events had taken place, thereby influencing isotopic values.

4.3. Overall conditions at the Cedars result in isotopic disequilibrium

Several factors control the expression of KIEs in carbonate minerals from The Cedars. These include the hydroxylation favored pathway, DIC speciation, increased rate of CO_2 uptake into the system, and mineral precipitation prior to isotopic equilibria. Because Type 1 and 2 waters are readily mixing at the surface, a hyperalkaline environment (pH > 11) is created due to excess OH^- anions present in Type 2 fluids. At a pH > 10, the hydroxylation pathway represents > 95% of reactions transforming CO_2 to HCO_3^- (McConnaughey, 1989). This high pH also creates an environment that facilitates rapid uptake of CO_2 into the aqueous media (Lerman and Stumm, 1989) due to the concentration gradient created by the DIC speciation preference of CO_3^{2-} at pH > 10 (Hill et al., 2014; Tripati et al., 2015). This condition, coupled with the rapid precipitation of $CaCO_3$ due to the high saturation state (Christensen et al., 2021), creates an even stronger gradient, further increasing the uptake of CO_2 from the atmosphere. The forward reaction rate associated with CO_2 hydroxylation is >1000 times the reverse reaction (Christensen et al., 2021), creating a pathway that is approximately unidirectional. We hypothesize this is preventing backwards conversion which is essential for O isotope exchange that would facilitate $\delta^{18}O$, Δ_{47}, and Δ_{48} equilibrium. The high pH results in a much greater equilibration time (>40 days) being required for the DIC pool to achieve clumped and oxygen isotopic equilibria prior to mineral precipitation (Beck et al., 2005; Tripati et al., 2015; Guo, 2020; Uchikawa et al., 2021). As the system moves into the deeper parts of the spring pool (below 100 μm), there are additional fluxes including advection and diffusion of Type 2 waters, $CaCO_3$ precipitation, and EIC contribution from the surface.

4.4. Examination of kinetic isotope effects using modeling

IsoDIC (Guo, 2020) modeling of disequilibria in the DIC pool used input parameters taken from the surface floe conditions of The Cedars and accurately predicted the measured range of Δ_{47} and Δ_{48} values (Fig. 6A). The model was used to predict the evolution of disequilibria associated with HCO_3^- and CO_3^{2-} with respect to residence time in the system. The model indicated a rapid departure away from equilibria

with maximum disequilibria achieved at ~1 h of DIC residence time. This initial departure rebounds back to equilibrium as the system has more time equilibrate, where equilibrium is eventually achieved after ~1000 h. Due to the low [CO_2] from DIC speciation favoring CO_3^{2-} at high pH (Beck et al., 2005; Tripati et al., 2015), the migration back to equilibria at these conditions is very slow. The IsoDIC (Guo, 2020) model can be used to predict the approximate timeframe associated with precipitation at the surface, which we hypothesize to be ≤1 h from when CO_2 is introduced into the surface spring system (Fig. 6A). A caveat is that this model only considers the KIEs associated with the DIC pool and does not factor those associated with mineral precipitation.

Since the IsoDIC model did not consider KIEs associated with mineral precipitation, isotopic evolution was also predicted with the COAD model, which does predict KIEs from precipitation, using the same input parameters as for the IsoDIC model. This model predicted a similar trend for Δ_{47} and Δ_{48} (Fig. 6B) when compared to the IsoDIC model, in terms of migration from equilibrium to disequilibrium. However, while the two models yield initial values for CO_3^{2-} and HCO_3^- that are very similar, these values deviate up to 0.1 ‰ from the KIEs associated with mineral precipitation. Additionally, the measured Δ_{47} values and COAD predictions are in good agreement (Fig. 6C), while some measured Δ_{48} values for travertine samples and snow samples collected from the bottom of the pool (Table 1) deviate from model predicted Δ_{48} values by up to 0.1‰ (Fig. 6D). The ancient travertine samples (T1, T2, T3a, T3b, T4, T5) contained multiple layers, and therefore mixing may impact clumped isotopes (Eiler and Schauble, 2004; Defliese and Lohmann, 2015), and there is no current knowledge of possible differences in travertine versus typical calcite Δ_{48} values. Mixing may also bias clumped isotope values in the snow samples, which may experience temporal variations in DIC isotopic composition. Further, some of the snow samples have mixed minerology (aragonite, calcite, brucite), such as samples PB-C1, PE-C2, and PE-C2 (Table 1). The brucite [$Mg(OH)_2$] composition ranges from 4% to 7%, which has unknown effects on acid digestion and potentially the clumped isotope values.

COAD modeling enables us to determine and predict the rates of mineral precipitation associated with the respective system, which is constrained by measured dual clumped isotope values. The COAD model was also used to predict the dependence of Δ_{47} and Δ_{48} values from The Cedars samples on the precipitation rate (Fig. 6E-F). The model accurately predicted the average Δ_{47} value at the BSC springs, given the measured precipitation rate (Christensen et al., 2021). Comparison of dual clumped data to model results supports a natural precipitation rate of $\sim 4.8 \times 10^{-7}$ mol/m^2/s (Fig. 6E). However, the model underpredicted the average Δ_{48} value (Fig. 6F). This may be due to greater measurement uncertainty for Δ_{48}, which is an order of magnitude greater than for Δ_{47} (1 SE for $\Delta_{47} \approx 0.001$ ‰; 1 SE for $\Delta_{48} \approx 0.01$ ‰), and no previous experimental constraints on how Δ_{48} values vary from increased precipitation rates.

We find the two models provide a slightly different set of tools. The IsoDIC model focuses on the time evolution of the isotopic composition of DIC species from an initially perturbed or disequilibrium state. In this framework, the steady state of the system is equivalent to the equilibrium state. By contrast, the COAD box model involves fluxes of CO_2 and $CaCO_3$ such that the isotopic composition of DIC species is continually perturbed. In this framework, the steady state of the system is not equivalent to the equilibrium state unless the CO_2 flux is extremely small compared to the size of the DIC pool. Using the COAD model, accurately measured Δ_{47} and Δ_{48} values can be compared to model predicted values as a function of the CO_2 influx and $CaCO_3$ outflux (i.e., mineral precipitation rate).

Field measurements and modeling may be useful for application to other peridotite bodies to help determine the natural mineral precipitation rates and DIC residence time. Our work here shows this approach is useful for predicting the natural rates of CO_2 uptake. If the rate of CO_2 uptake was enhanced using a feed of high-pressure CO_2 and hydraulic fracturing, dual clumped isotope measurements could be interpreted within a modeling framework to evaluate the enhanced rates of DIC equilibration and mineral formation.

4.5. Potential CO_2 sequestration application

Assuming the natural carbonation rate of peridotite consumes ~2 tons of CO_2/km^3/year (Kelemen and Matter, 2008), then the peridotite at The Cedars, surrounding ophiolite in the Coast Range, and ophiolite in Oman consume ~63, $\sim 1.1 \times 10^4$, and $\sim 4.2 \times 10^4$ tons of CO_2 per year, respectively (Fig. 7). At the natural rate, the peridotite at The Cedars would take $>10^8$ years to achieve the maximum CO_2 sequestration potential of $\sim 7.4 \times 10^8$ tons. The peridotite at the CRO and Oman would take $>10^{10}$ and $>10^{13}$ years to reach their CO_2 sequestrations potentials of $\sim 9.7 \times 10^{10}$ (Carnevale, 2013) and $\sim 7.7 \times 10^{13}$ (Kelemen and Matter, 2008) tons, respectively. While these ultramafic formations provide an important natural CO_2 sink, the total yearly sequestration represents ≪1% of current global CO_2 emissions of 34.9×10^9 tons (Liu et al., 2022).

Previous work by Kelemen and Matter (2008) proposed a method for enhanced *in situ* carbonation of peridotite for the Samail Ophiolite in Oman. This method increases the natural carbonation reaction (reaction (10)) rate by up to 10^6 times by drilling and hydraulic fracturing of the rock to increase the reactive surface area, initial heating of the rock to 185 °C using hot fluids, followed by the injection of CO_2 (pressure = 300 bars, temperature = 25 °C, flow rate = 0.040 m/s) (Kelemen and Matter, 2008). After the initial heating, the exothermic carbonation reaction maintains the system temperature at 185 °C (Kelemen and Matter, 2008). As the reactive surface becomes depleted, the rock may require additional fracturing, although some cracking may occur from the temperature changes and increases in solid volume from mineral hydration and carbonation (Kelemen and Matter, 2008). If we assume the fully catalyzed reaction rate of $\sim 2 \times 10^9$ tons CO_2/km^3/year, it would take <50 years and <40,000 years, respectively, for all Mg, Ca, and Fe in the CRO and Oman peridotite to be converted into carbonate minerals (Fig. 7). This would consume billions of tons of CO_2 per year.

Yet there are major potential environmental justice issues that are problematic. A hurdle to employing mineral carbonation technology in peridotite formations is that ~1 million drill holes (Kelemen et al., 2011) may be required to offset 34.9×10^9 tons (Liu et al., 2022) of anthropogenic CO_2 emissions per year. Further, these operations could result in deforestation (Drohan and Brittingham, 2012), loss of wildlife habitats (Kiviat, 2013), and contaminated wells (Holzman, 2011), as has been observed with fracking. The latter could potentially strain water resources, and have negative impacts on human and environmental health. While it is notable that the in-situ CO_2 sequestration potential in peridotite bodies is high when compared to other potential technologies, the potential short and long-term consequences need to be considered. High-temperature mineral carbonation reactors, which would use mineral feedstock from mines and direct CO_2 injection, could rapidly convert serpentine and olivine to magnesite and quartz, resulting in $\sim 8.8 \times 10^5$ to $\sim 8.8 \times 10^6$ tons of CO_2 sequestered per year (Power et al., 2013). The injection of CO_2 into ponds containing serpentinite mine tailings could sequester up to $\sim 1 \times 10^6$ tons of CO_2 per year (Power et al., 2013). This may be enhanced if the ponds utilize photoautotrophic microbes, such as algae and cyanobacteria, which use CO_2 as an energy source (Power et al., 2011). Yet associated land use and biosphere changes could negatively impact emissions reduction, and the adverse effects on water and environmental health may counter potential benefits. It is likely that multiple strategies will need to be used in parallel to reach global carbon dioxide reduction goals, which are 10 Gt/yr by 2050 and 20 Gt/yr by 2100 (UNEP, 2019), and the breadth of consequences of each approach should be carefully assessed before moving forward with implementation.

5. Conclusions

We analyzed carbonate mineral samples collected from springs at The Cedars, a peridotite body in Northern California, for dual clumped and bulk stable isotopes. We combined measured Δ_{47}, Δ_{48}, $\delta^{18}O$, and $\delta^{13}C$ and model calculations to study kinetic isotope effects associated with CO_2 absorption, high pH, and precipitation rate. Our work suggests kinetic biases in dual clumped and bulk isotope values arise due to carbonate mineral precipitation from highly alkaline waters through a CO_2 absorption-driven pathway. Our analysis indicates that the largest KIEs are from samples recovered from surface floes. In surface floes, there is sufficient contact between the spring waters and the atmosphere where CO_2 absorption and rapid precipitation conditions are favored. Modern samples with isotopic values within error of equilibrium occur in locations where there is significant mixing of surface and spring waters. Other samples with kinetically biased isotopic values include "snow" samples recovered from the bottom of springs and ancient travertine samples. We report slopes (Δ_{48}/Δ_{47}, $\Delta_{47}/\delta^{18}O$, $\Delta_{48}/\delta^{18}O$, $\Delta_{47}/\delta^{13}C$, $\Delta_{48}/\delta^{13}C$) for CO_2 (de)hydration and (de)hydroxylation disequilibria processes from The Cedars samples. The slopes are consistent with $\Delta_{47}/\delta^{18}O$ and $\Delta_{47}/\delta^{13}C$ slopes from a peridotite body in Oman, as well as modeling predictions for KIEs from CO_2 (de)hydration and (de) hydroxylation.

This work sets up the potential use of the Δ_{47}-Δ_{48} dual clumped isotope method, combined with modeling, to examine sites of interest for geological CO_2 sequestration, including in the Coast Ranges and other peridotite bodies. This relatively non-invasive method can be used to determine the natural rate of CO_2 uptake, mineral precipitation rate, and for determining evolution time and (dis)equilibria in DIC. We recommend expansion of dual clumped isotope research into carbonate minerals precipitating from peridotite veins to compare surface and subsurface processes, and better understand the feasibility of sites for CO_2 sequestration, alongside assessment of the potential adverse environmental and human health impacts of implementation in different locations.

Declaration of Competing Interest

The authors declare that they have no known competing financial interests or personal relationships that could have appeared to influence the work reported in this paper.

Data availability

Replicate data for samples and standards, statistical analyses of standards, parameters used in CO_2 sequestration calculations, information about clumped isotope data quality assurance, and model codes are available through Zenodo at https://doi.org/10.5281/zenodo.8136571.

Acknowledgments

We thank the reviewers and editor for their helpful suggestions and thoughtful handling of the manuscript. We thank lab members past and present for their work running standards, efforts in data entry, and contributions to discussions. We thank Jade Knighton and Adiba Hassan for their support. This work was funded by the United States Department of Energy, Office of Basic Energy Sciences (DOE BES) grant DE-FG02-83613ER16402, Heising-Simons Foundation grant 2022-3314, NSF grant ICER- 2039462 for Veterans in STEM, and a Royal Society Wolfson Visiting Fellowship to Aradhna Tripati. Zeeshan Parvez, Jamie Lucarelli, Irvin Matamoros, Joshua Rubi, Kevin Miguel, Randy Flores, and Robert Ulrich acknowledge support from the above grants and from fellowships by The Center for Diverse Leadership in Science which is supported by the Packard Foundation, Sloan Foundation, Silicon Valley Community Foundation, and NSF. Zeeshan Parvez received support as a Tillman Scholar. Jamie Lucarelli received support from Cota Robles and Dissertation Year Fellowships from the University of California, Los Angeles. We thank Ben Elliot and members of the Eagle-Tripati laboratory for their technical support in mass spectrometry. James Watkins was supported by the National Science Foundation under Grant No. EAR1749183. Support to John Christensen was provided by the United States Department of Energy, Office of Basic Energy Sciences (DOE BES) under Award # DE-AC02-05CHii231 to Lawrence Berkeley National Laboratory. AT initiated and supported the work. AT and JC designed the research. ZP and JL wrote the manuscript with guidance from AT and RE and input from all coauthors. JC provided samples. JL, ZP, IM, JR, KM, BE, RF performed the isotope analyses and calculations with input from AT. ZP performed the IsoDIC and COAD model calculations. JL performed the CO_2 sequestration calculations. JW modified the COAD model for this project and provided training for implementation and post-processing. ZP, JL, RU, RE contributed insights to data analyses and interpretations. AT and RE advised ZP, IM, JR, KM, RF, JL, and RU.

Appendix A. Supplementary material

The Supplementary Material contains figures demonstrating instrument performance and standard values used in data corrections, and equations and parameters used for modeling. Supplementary data to this article can be found online at https://doi.org/10.1016/j.gca.2023.06.022.

References

Affek, H.P., Bar-Matthews, M., Ayalon, A., Matthews, A., Eiler, J.M., 2008. Glacial/interglacial temperature variations in Soreq cave speleothems as recorded by 'clumped isotope' thermometry. Geochim. Cosmochim. Acta 72, 5351–5360.

Anderson, N.T., Kelson, J.R., Kele, S., Daëron, M., Bonifacie, M., Horita, J., Mackey, T.J., John, C.M., Kluge, T., Petschnig, P., Jost, A.B., Huntington, K.W., Bernasconi, S.M., Bergmann, K.D., 2021. A Unified Clumped Isotope Thermometer Calibration (0.5–1,100°C) Using Carbonate-Based Standardization. Geophys. Res. Lett. 48.

Bajnai, D., Guo, W., Spötl, C., Coplen, T.B., Methner, K., Löffler, N., Krsnik, E., Gischler, E., Hansen, M., Henkel, D., Price, G.D., Raddatz, J., Scholz, D., Fiebig, J., 2020. Dual clumped isotope thermometry resolves kinetic biases in carbonate formation temperatures. Nat. Commun. 11, 4005.

Barnes, I., O'Neil, J.R., 1969. The Relationship between Fluids in Some Fresh Alpine-Type Ultramafics and Possible Modern Serpentinization, Western United States. Geol. Soc. Am. Bull. 80, 1947.

Beck, W.C., Grossman, E.L., Morse, J.W., 2005. Experimental studies of oxygen isotope fractionation in the carbonic acid system at 15°, 25°, and 40°C. Geochim. Cosmochim. Acta 69, 3493–3503.

Bernasconi, S.M., Müller, I.A., Bergmann, K.D., Breitenbach, S.F.M., Fernandez, A., Hodell, D.A., Jaggi, M., Meckler, A.N., Millan, I., Ziegler, M., 2018. Reducing Uncertainties in Carbonate Clumped Isotope Analysis Through Consistent Carbonate-Based Standardization. Geochem. Geophys. Geosyst. 19, 2895–2914.

Bernasconi, S.M., Daëron, M., Bergmann, K.D., Bonifacie, M., Meckler, A.N., Affek, H.P., Anderson, N., Bajnai, D., Barkan, E., Beverly, E., Blamart, D., Burgener, L., Calmels, D., Chaduteau, C., Clog, M., Davidheiser-Kroll, B., Davies, A., Dux, F., Eiler, J., Elliott, B., Fetrow, A.C., Fiebig, J., Goldberg, S., Hermoso, M., Huntington, K.W., Hyland, E., Ingalls, M., Jaggi, M., John, C.M., Jost, A.B., Katz, S., Kelson, J., Kluge, T., Kocken, I.J., Laskar, A., Leutert, T.J., Liang, D., Lucarelli, J., Mackey, T.J., Mangenot, X., Meinicke, N., Modestou, S.E., Müller, I.A., Murray, S., Neary, A., Packard, N., Passey, B.H., Pelletier, E., Petersen, S., Piasecki, A., Schauer, A., Snell, K.E., Swart, P.K., Tripati, A., Upadhyay, D., Vennemann, T., Winkelstern, I., Yarian, D., Yoshida, N., Zhang, N., Ziegler, M., 2021. InterCarb: A Community Effort to Improve Interlaboratory Standardization of the Carbonate Clumped Isotope Thermometer Using Carbonate Standards. Geochem. Geophys. Geosyst. 22 (5).

Blake, M.C., Bailey, E.H., Wentworth, C.M., 2012. The Cedars Ultramafic Mass, Sonoma County, California. USGS Open-File Rep. 2012–1164, 1–16.

Brand, W.A., Assonov, S.S., Coplen, T.B., 2010. Correction for the ^{17}O interference in $\delta^{13}C$ measurements when analyzing CO_2 with stable isotope mass spectrometry (IUPAC Technical Report). Pure Appl. Chem. 82, 1719–1733.

Bruni, J., Canepa, M., Chiodini, G., Cioni, R., Cipolli, F., Longinelli, A., Marini, L., Ottonello, G., Vetuschi, Z.M., 2002. Irreversible water-rock mass transfer accompanying the generation of the neutral, Mg-HCO_3 and high-pH, Ca-OC spring waters of the Genova province. Italy. Appl. Geochem. 17, 455–474.

Carnevale, D.C., 2013. Carbon sequestration potential of the Coast Range Ophiolite in California. University of Rhode Island ProQuest Dissertations Publishing.

Chen, S., Gagnon, A.C., Adkins, J.F., 2018. Carbonic anhydrase, coral calcification and a new model of stable isotope vital effects. Geochim. Cosmochim. Acta 236, 179–197.

Christensen, J.N., Watkins, J.M., Devriendt, L.S., DePaolo, D.J., Conrad, M.E., Voltolini, M., Yang, W., Dong, W., 2021. Isotopic fractionation accompanying CO_2 hydroxylation and carbonate precipitation from high pH waters at The Cedars, California, USA. Geochim. Cosmochim. Acta 301, 91–115.

Cipolli, F., Gambardella, B., Marini, L., Ottonello, G., Vetuschi Zuccolini, M., 2004. Geochemistry of high-pH waters from serpentinites of the Gruppo di Voltri (Genova, Italy) and reaction path modeling of CO_2 sequestration in serpentinite aquifers. Appl. Geochem. 19, 787–802.
Coleman, R.G., 2000. Prospecting for ophiolites along the California continental margin. Geol. Soc. Am. Special Pap. 349, 351–364.
Coleman, R.G., 2004. Geologic Nature of the Jasper Ridge Biological Preserve, San Francisco Peninsula, California. Int. Geol. Rev. 46, 629–637.
Daëron, M., Blamart, D., Peral, M., Affek, H.P., 2016. Absolute isotopic abundance ratios and the accuracy of Δ_{47} measurements. Chem. Geol. 442, 83–96.
de Obeso, J.C., Kelemen, P.B., 2018. Fluid rock interactions on residual mantle peridotites overlain by shallow oceanic limestones: Insights from Wadi Fins, Sultanate of Oman. Chem. Geol. 498, 139–149.
Defliese, W.F., Lohmann, K.C., 2015. Non-linear mixing effects on mass-47 CO_2 clumped isotope thermometry: Patterns and implications: Non-linear mixing effects on mass-47 clumped isotopes. Rapid Commun. Mass Spectrom. 29, 901–909.
Dennis, K.J., Affek, H.P., Passey, B.H., Schrag, D.P., Eiler, J.M., 2011. Defining an absolute reference frame for 'clumped' isotope studies of CO_2. Geochim. Cosmochim. Acta 75, 7117–7131.
Devriendt, L.S., Watkins, J.M., McGregor, H.V., 2017. Oxygen isotope fractionation in the $CaCO_3$-DIC-H_2O system. Geochim. Cosmochim. Acta 214, 115–142.
Dietzel, M., Tang, J., Leis, A., Köhler, S.J., 2009. Oxygen isotopic fractionation during inorganic calcite precipitation – Effects of temperature, precipitation rate and pH. Chem. Geol. 268, 107–115.
Drohan, P.J., Brittingham, M., 2012. Topographic and Soil Constraints to Shale-Gas Development in the Northcentral Appalachians. Soil Sci. Soc. Am. J. 76, 1696–1706.
Eiler, J.M., 2007. "Clumped-isotope" geochemistry—The study of naturally-occurring, multiply-substituted isotopologues. Earth Planet. Sci. Lett. 262, 309–327.
Eiler, J.M., Schauble, E., 2004. $^{18}O^{13}C^{16}O$ in Earth's atmosphere. Geochim. Cosmochim. Acta 68, 4767–4777.
Falk, E.S., Guo, W., Paukert, A.N., Matter, J.M., Mervine, E.M., Kelemen, P.B., 2016. Controls on the stable isotope compositions of travertine from hyperalkaline springs in Oman: Insights from clumped isotope measurements. Geochim. Cosmochim. Acta 192, 1–28.
Fiebig, J., Bajnai, D., Löffler, N., Methner, K., Krsnik, E., Mulch, A., Hofmann, S., 2019. Combined high-precision Δ_{48} and Δ_{47} analysis of carbonates. Chem. Geol. 522, 186–191.
Fiebig, J., Daëron, M., Bernecker, M., Guo, W., Schneider, G., Boch, R., Bernasconi, S.M., Jautzy, J., Dietzel, M., 2021. Calibration of the dual clumped isotope thermometer for carbonates. Geochim. Cosmochim. Acta, S0016703721004208.
García del Real, P., Maher, K., Kluge, T., Bird, D.K., Brown, G.E., John, C.M., 2016. Clumped-isotope thermometry of magnesium carbonates in ultramafic rocks. Geochim. Cosmochim. Acta 193, 222–250.
Ghosh, P., Adkins, J., Affek, H., Balta, B., Guo, W., Schauble, E.A., Schrag, D., Eiler, J.M., 2006. ^{13}C–^{18}O bonds in carbonate minerals: A new kind of paleothermometer. Geochim. Cosmochim. Acta 70, 1439–1456.
Guo, W., 2020. Kinetic clumped isotope fractionation in the DIC-H_2O-CO_2 system: Patterns, controls, and implications. Geochim. Cosmochim. Acta 268, 230–257.
Guo, W., Mosenfelder, J.L., Goddard, W.A., Eiler, J.M., 2009. Isotopic fractionations associated with phosphoric acid digestion of carbonate minerals: Insights from first-principles theoretical modeling and clumped isotope measurements. Geochim. Cosmochim. Acta 73, 7203–7225.
Guo, W., Zhou, C., 2019. Patterns and controls of disequilibrium isotope effects in speleothems: Insights from an isotope-enabled diffusion-reaction model and implications for quantitative thermometry. Geochim. Cosmochim. Acta 267, 196–226.
Hendy, C.H., 1971. The isotopic geochemistry of speleothems—I. The calculation of the effects of different modes of formation on the isotopic composition of speleothems and their applicability as palaeoclimatic indicators. Geochim. Cosmochim. Acta 35, 801–824.
Henkes, G.A., Passey, B.H., Wanamaker, A.D., Grossman, E.L., Ambrose, W.G., Carroll, M.L., 2013. Carbonate clumped isotope compositions of modern marine mollusk and brachiopod shells. Geochim. Cosmochim. Acta 106, 307–325.
Hill, P.S., Tripati, A.K., Schauble, E.A., 2014. Theoretical constraints on the effects of pH, salinity, and temperature on clumped isotope signatures of dissolved inorganic carbon species and precipitating carbonate minerals. Geochim. Cosmochim. Acta 125, 610–652.
Hill, P.S., Schauble, E.A., Tripati, A., 2020. Theoretical constraints on the effects of added cations on clumped, oxygen, and carbon isotope signatures of dissolved inorganic carbon species and minerals. Geochim. Cosmochim. Acta 269, 496–539.
Holzman, D.C., 2011. Methane Found in Well Water Near Fracking Sites. Environ. Health Perspect. 119.
John, C.M., Bowen, D., 2016. Community software for challenging isotope analysis: First applications of 'Easotope' to clumped isotopes: Community software for challenging isotope analysis. Rapid Commun. Mass Spectrom. 30, 2285–2300.
Kastrinakis, A., Skliros, V., Tsakiridis, P., Perraki, M., 2021. CO_2-Mineralised Nesquehonite: A New "Green" Building Material. In International Conference on Raw Materials and Circular Economy RawMat 2021. MDPI. p. 60.
Kelemen, P.B., Matter, J., 2008. In situ carbonation of peridotite for CO_2 storage. Proc. Natl. Acad. Sci. 105, 17295–17300.
Kelemen, P.B., Matter, J., Streit, E.E., Rudge, J.F., Curry, W.B., Blusztajn, J., 2011. Rates and Mechanisms of Mineral Carbonation in Peridotite: Natural Processes and Recipes for Enhanced, in situ CO_2 Capture and Storage. Annu. Rev. Earth Planet. Sci. 39, 545–576.
Kim, S.-T., O'Neil, J.R., 1997. Equilibrium and nonequilibrium oxygen isotope effects in synthetic carbonates. Geochim. Cosmochim. Acta 61, 3461–3475.
Kim, S.-T., O'Neil, J.R., Hillaire-Marcel, C., Mucci, A., 2007. Oxygen isotope fractionation between synthetic aragonite and water: Influence of temperature and Mg^{2+} concentration. Geochim. Cosmochim. Acta 71, 4704–4715.
Kiviat, E., 2013. Risks to biodiversity from hydraulic fracturing for natural gas in the Marcellus and Utica shales: Hydraulic fracturing and biodiversity. Ann. N. Y. Acad. Sci. 1286, 1–14.
Lerman, A., Stumm, W., 1989. CO_2 storage and alkalinity trends in lakes. Water Res. 23, 139–146.
Liu, Z., Deng, Z., Davis, S.J., Giron, C., Ciais, P., 2022. Monitoring global carbon emissions in 2021. Nat. Rev. Earth Environ. 3, 217–219.
Lívanský, K., 1982. Effect of temperature and pH on absorption of carbon dioxide by a free level of mixed solutions of some buffers. Folia Microbiol. (Praha) 27, 55–59.
Lucarelli, J.K., Carroll, H.M., Ulrich, R.N., Elliott, B.M., Coplen, T.B., Eagle, R.A., Tripati, A., 2023. Equilibrated Gas and Carbonate Standard-Derived Dual (Δ_{47} and Δ_{48}) Clumped Isotope Values. Geochem. Geophys. Geosyst. 24 (2).
Matter, J.M., Kelemen, P.B., 2009. Permanent storage of carbon dioxide in geological reservoirs by mineral carbonation. Nat. Geosci. 2, 837–841.
McConnaughey, T., 1989. ^{13}C and ^{18}O isotopic disequilibrium in biological carbonates: II. In vitro simulation of kinetic isotope effects. Geochim. Cosmochim. Acta 53, 163–171.
McDermott, F., Atkinson, T.C., Fairchild, I.J., Baldini, L.M., Mattey, D.P., 2011. A first evaluation of the spatial gradients in $\delta^{18}O$ recorded by European Holocene speleothems. Glob. Planet. Change 79, 275–287.
Moody, J.B., 1976. Serpentinization: a review. Lithos 9, 125–138.
Morrill, P.L., Kuenen, J.G., Johnson, O.J., Suzuki, S., Rietze, A., Sessions, A.L., Fogel, M. L., Nealson, K.H., 2013. Geochemistry and geobiology of a present-day serpentinization site in California: The Cedars. Geochim. Cosmochim. Acta 109, 222–240.
Passey, B.H., Levin, N.E., Cerling, T.E., Brown, F.H., Eiler, J.M., 2010. High-temperature environments of human evolution in East Africa based on bond ordering in paleosol carbonates. Proc. Natl. Acad. Sci. 107, 11245–11249.
Power, I.M., Wilson, S.A., Dipple, G.M., 2013. Serpentinite Carbonation for CO_2 Sequestration. Elements 9, 115–121.
Power, I.M., Wilson, S.A., Small, D.P., Dipple, G.M., Wan, W., Southam, G., 2011. Microbially Mediated Mineral Carbonation: Roles of Phototrophy and Heterotrophy. Environ. Sci. Technol. 45, 9061–9068.
Saenger, C., Affek, H.P., Felis, T., Thiagarajan, N., Lough, J.M., Holcomb, M., 2012. Carbonate clumped isotope variability in shallow water corals: Temperature dependence and growth-related vital effects. Geochim. Cosmochim. Acta 99, 224–242.
Schauble, E.A., Ghosh, P., Eiler, J.M., 2006. Preferential formation of ^{13}C–^{18}O bonds in carbonate minerals, estimated using first-principles lattice dynamics. Geochim. Cosmochim. Acta 70, 2510–2529.
Schefer, J., Grube, M., 1995. Low temperature structure of magnesium nitrate hexahydrate, $Mg(NO_3)_2{\cdot}6H_2O$: A neutron diffraction study at 173 K. Mater. Res. Bull. 30, 1235–1241.
Sleep, N.H., Meibom, A., Fridriksson, T.h., Coleman, R.G., Bird, D.K., 2004. H_2-rich fluids from serpentinization: Geochemical and biotic implications. Proc. Natl. Acad. Sci. 101, 12818–12823.
Spooner, P.T., Guo, W., Robinson, L.F., Thiagarajan, N., Hendry, K.R., Rosenheim, B.E., Leng, M.J., 2016. Clumped isotope composition of cold-water corals: A role for vital effects? Geochim. Cosmochim. Acta 179, 123–141.
Suzuki, S., Ishii, S., Hoshino, T., Rietze, A., Tenney, A., Morrill, P.L., Inagaki, F., Kuenen, J.G., Nealson, K.H., 2017. Unusual metabolic diversity of hyperalkaliphilic microbial communities associated with subterranean serpentinization at the Cedars. ISME J. 11, 2584–2598.
Swart, P.K., Lu, C., Moore, E.W., Smith, M.E., Murray, S.T., Staudigel, P.T., 2021. A calibration equation between Δ_{48} values of carbonate and temperature. Rapid Commun. Mass Spectrom. 35.
Tang, J., Dietzel, M., Fernandez, A., Tripati, A.K., Rosenheim, B.E., 2014. Evaluation of kinetic effects on clumped isotope fractionation (Δ_{47}) during inorganic calcite precipitation. Geochim. Cosmochim. Acta 134, 120–136.
Thiagarajan, N., Adkins, J., Eiler, J., 2011. Carbonate clumped isotope thermometry of deep-sea corals and implications for vital effects. Geochim. Cosmochim. Acta 75, 4416–4425.
Tripati, A.K., Hill, P.S., Eagle, R.A., Mosenfelder, J.L., Tang, J., Schauble, E.A., Eiler, J. M., Zeebe, R.E., Uchikawa, J., Coplen, T.B., Ries, J.B., Henry, D., 2015. Beyond temperature: Clumped isotope signatures in dissolved inorganic carbon species and the influence of solution chemistry on carbonate mineral composition. Geochim. Cosmochim. Acta 166, 344–371.
Uchikawa, J., Chen, S., Eiler, J.M., Adkins, J.F., Zeebe, R.E., 2021. Trajectory and timescale of oxygen and clumped isotope equilibration in the dissolved carbonate system under normal and enzymatically-catalyzed conditions at 25 °C. Geochim. Cosmochim. Acta 314, 313–333.
Uchikawa, J., Zeebe, R.E., 2012. The effect of carbonic anhydrase on the kinetics and equilibrium of the oxygen isotope exchange in the CO_2–H_2O system: Implications for $\delta^{18}O$ vital effects in biogenic carbonates. Geochim. Cosmochim. Acta 95, 15–34.
United Nations Environment Programme, 2019. Emissions Gap Report 2018.
Upadhyay, D., Lucarelli, J., Arnold, A., Flores, R., Bricker, H., Ulrich, R.N., Jesmok, G., Santi, L., Defliese, W., Eagle, R.A., Carroll, H.M., Bateman, J.B., Petryshyn, V., Loyd, S.J., Tang, J., Priyadarshi, A., Elliott, B., Tripati, A., 2021. Carbonate clumped isotope analysis (Δ_{47}) of 21 carbonate standards determined via gas-source isotope-ratio mass spectrometry on four instrumental configurations using carbonate-based standardization and multiyear data sets. Rapid Commun. Mass Spectrom. 35.
Usdowski, E., Michaelis, J., Boettcher, M., Hoefs, J., 1991. Factors for the oxygen isotope equilibrium fractionation between aqueous and gaseous CO_2, carbonic acid,

bicarbonate, carbonate, and water (19°C). Z. Phys. Chem.-Int. J. Res. Phys. Chem. Chem. Phys. 170, 237–249.
Watkins, J., Devriendt, L., 2022. A combined model for kinetic clumped isotope effects in the $CaCO_3$-DIC-H_2O system. Geochem. Geophys. Geosyst. 23 (8).
Watkins, J.M., Hunt, J.D., 2015. A process-based model for non-equilibrium clumped isotope effects in carbonates. Earth Planet. Sci. Lett. 432, 152–165.
Weise, A., Kluge, T., 2020. Isotope exchange rates in dissolved inorganic carbon between 40 °C and 90 °C. Geochim. Cosmochim. Acta 268, 56–72.
Zedef, V., Russell, M.J., Fallick, A.E., Hall, A.J., 2000. Genesis of Vein Stockwork and Sedimentary Magnesite and Hydromagnesite Deposits in the Ultramafic Terranes of Southwestern Turkey: A Stable Isotope Study. Econ. Geol. 95, 429–445.
Zeebe, R.E., Wolf-Gladrow, D.A., 2001. CO_2 in Seawater: Equilibrium, Kinetics, Isotopes. Elsevier, Amsterdam, New York.